

This article appeared in a journal published by Elsevier. The attached copy is furnished to the author for internal non-commercial research and education use, including for instruction at the authors institution and sharing with colleagues.

Other uses, including reproduction and distribution, or selling or licensing copies, or posting to personal, institutional or third party websites are prohibited.

In most cases authors are permitted to post their version of the article (e.g. in Word or Tex form) to their personal website or institutional repository. Authors requiring further information regarding Elsevier's archiving and manuscript policies are encouraged to visit:

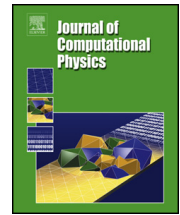
<http://www.elsevier.com/authorsrights>



Contents lists available at ScienceDirect

## Journal of Computational Physics

www.elsevier.com/locate/jcp



# Computation of probabilistic hazard maps and source parameter estimation for volcanic ash transport and dispersion



R. Madankan<sup>a</sup>, S. Pouget<sup>b</sup>, P. Singla<sup>a,\*</sup>, M. Bursik<sup>b</sup>, J. Dehn<sup>e</sup>, M. Jones<sup>c</sup>,  
A. Patra<sup>a</sup>, M. Pavolonis<sup>f</sup>, E.B. Pitman<sup>d</sup>, T. Singh<sup>a</sup>, P. Webley<sup>e</sup>

<sup>a</sup> Department of Mechanical & Aerospace Engineering, University at Buffalo, United States

<sup>b</sup> Department of Geology, University at Buffalo, United States

<sup>c</sup> Center for Computational Research, University at Buffalo, United States

<sup>d</sup> Department of Mathematics, University at Buffalo, United States

<sup>e</sup> Geophysical Institute, University of Alaska, Fairbanks, United States

<sup>f</sup> NOAA-NESDIS, Center for Satellite Applications and Research, United States

## ARTICLE INFO

### Article history:

Received 21 May 2013

Received in revised form 8 November 2013

Accepted 24 November 2013

Available online 6 December 2013

### Keywords:

Inverse problem

Source parameter estimation

Polynomial chaos

Minimum variance estimator

Hazard map

## ABSTRACT

Volcanic ash advisory centers are charged with forecasting the movement of volcanic ash plumes, for aviation, health and safety preparation. Deterministic mathematical equations model the advection and dispersion of these plumes. However initial plume conditions – height, profile of particle location, volcanic vent parameters – are known only approximately at best, and other features of the governing system such as the windfield are stochastic. These uncertainties make forecasting plume motion difficult. As a result of these uncertainties, ash advisories based on a deterministic approach tend to be conservative, and many times over/under estimate the extent of a plume. This paper presents an end-to-end framework for generating a probabilistic approach to ash plume forecasting. This framework uses an ensemble of solutions, guided by Conjugate Unscented Transform (CUT) method for evaluating expectation integrals. This ensemble is used to construct a polynomial chaos expansion that can be sampled cheaply, to provide a probabilistic model forecast. The CUT method is then combined with a minimum variance condition, to provide a full posterior pdf of the uncertain source parameters, based on observed satellite imagery. The April 2010 eruption of the Eyjafjallajökull volcano in Iceland is employed as a test example. The puff advection/dispersion model is used to hindcast the motion of the ash plume through time, concentrating on the period 14–16 April 2010. Variability in the height and particle loading of that eruption is introduced through a volcano column model called bent. Output uncertainty due to the assumed uncertain input parameter probability distributions, and a probabilistic spatial-temporal estimate of ash presence are computed.

© 2013 Elsevier Inc. All rights reserved.

## 1. Introduction

Ash clouds are produced by the explosive eruptions of volcanoes. These clouds, propagating downwind from a volcano eruption column, are a hazard to aircraft, causing damage to the engines [1]. On December 15, 1989, KLM Flight 867 lost all its engines when the airplane entered a plume of ash originating at the Redoubt volcano in the Aleutian Islands [2].

\* Corresponding author.

E-mail address: [psingla@buffalo.edu](mailto:psingla@buffalo.edu) (P. Singla).

That incident caused more than \$80 million (US) in damage to the aircraft, but fortunately no lives were lost. The recent eruption of the Eyjafjallajökull volcano in Iceland wreaked havoc on European aviation after the eruption started on April 14, 2010. Decisions about the closure of European air-space, largely based on deterministic ash plume models, resulted in more than \$4 billion in economic losses and left more than 10 million stranded passengers [3]. In addition to the large financial consequences of volcanic eruptions, there are significant health and environmental consequences of ash propagation and its subsequent fallout, ranging from inhalation of the ash particles to crop damage from tephra fallout. Clearly, those charged with volcanic risk management need accurate information for decision making. Among other components, this information flow should include a map of the probability of ash being present at a given location at a specified time.

Other hazardous events present similar needs. For example, the accidental release of radioactive gaseous material, such as occurred at the Chernobyl nuclear reactor explosion, or the oil spill resulting from the Deepwater Horizon accident in Gulf of Mexico, also demand tools and approaches, to accurately forecast the advection and dispersion of a material.

The primary objective of this work is to present an accurate and computationally efficient method to create probabilistic hazard maps for ash plume motion, which quantifies the uncertainties present in any model of ash advection and dispersion, and which integrates observation data whenever it is available. Providing such a map will enable public safety officials to make better decisions.

To be computationally tractable, the probabilistic framework presented here relies on a recently developed Conjugate Unscented Transformation (CUT) methodology to efficiently compute expectation integrals [4–7]. A linear unbiased minimum variance estimator is used in conjunction with the CUT methodology to provide estimates for source parameters and the associated uncertainty. A polynomial chaos-based emulation model is then used to compute a hazard map. Finally, numerical experiments are performed using data from the Eyjafjallajökull eruption, to validate the proposed methodology.

### 1.1. Current approaches and limitations

Often times volcanologists extrapolate information from past eruptions to create maps forecasting future events and areas at risk. Basing forecasts solely on past recorded events does not always provide a reliable estimate of likely eruption scenarios – prior events may have gone unreported, and site-specific conditions may have changed. Computer simulations using physics-based model equations, calibrated using field data, provide additional information on which to base hazard forecasts. To predict ash cloud movement, model systems may incorporate stochastic variability, such as uncertainty in source parameters or randomly varying wind fields, to better capture possible ash particle transport. A major source of uncertainty impacting the location of a volcanic ash cloud are the characteristics of the volcanic eruption column, including the distribution of grain size in the column and the column rise height [8]. Several investigations have tried to quantify the effect of source parameter uncertainty on the position of ash clouds. For example, during the Eyjafjallajökull eruption, the London Volcanic Ash Advisory Centers (VAAC) used the NAME computational model [9] for ash advection/dispersion to make forecasts of the position of the ash cloud, which in turn were used to issue advisories to the airline industry. In related work, Devenish et al. [10] applied NAME, with a specified set of input source parameters estimated from measurement data, to study the arrival of the Eyjafjallajökull ash cloud over the United Kingdom. Through a sensitivity analysis, this study demonstrated that the position and concentration of ash over a given region of interest were particularly dependent on eruption source parameters such as the column height and the particle profile within the column. O'Dowd et al. [11] simulated the dispersion of ash from Eyjafjallajökull using the REMOTE computational model, for a specified set of source parameters. In another study, Webley et al. [12] used the WRF-Chem dispersion and tracking model to forecast the ash cloud position, given the column height, particle grain-size distribution and mass eruption rate. Heinold et al. [13] simulated the Eyjafjallajökull emission, transport, and particle deposition over Europe by using the regional chemistry-transport model COSMO-MUSCAT, given the height of ash particles and their size distribution. Dispersion of the ash cloud from the Eyjafjallajökull eruption has also been simulated by using the FALL3D computational model [14], where the input parameters are approximated from the observed height of the eruption column and from the total grain size distribution as reconstructed from field observations. These investigations each apply different computational models to forecast ash cloud position as a function of time, each with its successes and limitations. In each instance, however, a specified set of the eruption source parameters, perhaps obtained retrospectively from radar or satellite data, is used to forecast ash cloud motion. Because there is great uncertainty in the model inputs, deterministic physics based models alone are limited in their ability to make meaningful forecasts.

In order to make accurate long-term forecasts, it is necessary to understand how the uncertainty in source parameters and the variability of wind fields propagate through the numerical advection/dispersion codes. Although a detailed sensitivity analysis can relate the variations in source parameters and wind data to ash cloud motion, uncertainty analysis provides a richer suite of tools, allowing an assessment of one's confidence in making forecasts based on all available information. Of course a successful application of uncertainty analysis must overcome the challenges posed by the large number of uncertain input parameters and the associated cost of computation. Data input and output drive the calculations of uncertainty quantification, and present additional difficulties for any analysis. Importantly, in real-time hazard assessment one is constrained by the need for rapid analysis. Each of these factors affects the trade-off between completeness and speed. In addition, propagating uncertain model inputs leads to forecasts with uncertainties that grow in time and which must be tamed in order to make useful forecasts; assimilating available observational data to refine the model forecast reduces these uncertainties.

Surprisingly, limited research has been done on fusing model forecasts with available measurement data to accurately forecast ash cloud motion. The exceptions are the recent works of Stohl et al., Denlinger et al. and Kristiansen et al. [15–17], who use inversion methods to couple *a-priori* source information and the output of dispersion models together with satellite data, to estimate volcanic source parameters. As a consequence, simulations performed by using these *posterior* source estimates result in better correspondence with satellite data. The major drawback of this approach is that the inversion method results in a deterministic *point estimate* for the posterior values of source parameters, and completely neglects prior information and inaccuracies in measurement data. An alternative to simply fitting the measurement data is to exploit sensor noise characteristics. A simple probabilistic approach is to apply a Maximum Likelihood Estimate (MLE) [18] to estimate the parameter values. However, the MLE also provides only point estimates and does not provide any information about one's confidence in those estimates.

A Bayesian method such as the Maximum *a posteriori* (MAP) estimation [19] combines a prior distribution together with information contained in measurements, to provide optimal estimates for source parameters. Like the MLE method, significant computational effort is required to solve the optimization problem resulting from the MAP approach, to determine optimal source parameters. This computational burden restricts the application of the method in large scale dynamical systems.

## 1.2. Our approach

A useful alternative is to employ a spectral representation of uncertain parameters and system states. These ideas have been developed through the use of a generalized polynomial chaos (gPC) expansion for random variables and stochastic processes. gPC is an extension of the polynomial chaos (PC) idea of Wiener [20], and has been used to quantify the forward propagation of uncertainty in dynamic problems [21,22]. gPC has been recently used in a Bayesian framework as part of a parameter estimation problem (these are also referred to as inverse problems) [23–25]. In one such application, Marzouk et al. [24] used a gPC expansion in conjunction with a Markov chain Monte Carlo (MCMC) technique, to find a point estimate for an uncertain source parameter, as a maximum posterior estimate. In a different approach, Li et al. [23] generated a large ensemble of realizations as part of an Ensemble Kalman filter (EnKF), each of which is updated within a gPC framework. In both of these examples, the gPC formulation is used to propagate state or parameter uncertainty through a dynamic system of equations. Both examples involve the computation of projection and/or expectation integrals. The numerical error and computational complexity of the gPC approach stems from numerical quadrature schemes used to compute these integrals. Often times Gaussian quadrature methods are used in these calculations. Unfortunately the numerical accuracy of the Gauss quadrature scheme cannot be easily refined without incurring an exponential increase in computational cost. As an alternative, sparse grid quadrature schemes or Smolyak quadrature schemes require fewer computational points than do Gauss quadrature rules for the same accuracy. But sparse grid and Smolyak schemes introduce negative weights into the quadrature calculations, a feature that can cause difficulties with convergence, especially the convergence of higher order moments [26,27].

In contrast to all of these approaches, this paper presents an end-to-end process for generating probabilistic maps of atmospheric ash. Fig. 1 outlines our basic approach. Past knowledge of similar eruption and eruption source observation are used to create an initial probability distribution of the model parameters, for a recently developed model that couples a volcanic eruption column (the *bent* model) with a volcanic ash transport and dispersion (VATD) model (*puff*) [28]. These distributions are then used to generate an ensemble of simulation runs, guided by a quadrature scheme recently introduced by Adurthi et al. [5–7] called the Conjugate Unscented Transform. The ensemble outcomes are then integrated to generate a probabilistic map of the ash distribution in space and time by constructing a polynomial chaos based surrogate model of the VATD model. As satellite imagery becomes available, this data is used to find a posterior estimate of the volcano source parameters, using a minimum variance estimator as part of the solution of an inverse problem. Furthermore, the satellite data is also used to improve the model parameter distribution by updating the polynomial chaos surrogate model. These refined source parameters estimates can then be used in subsequent propagation and forecast.

Although this paper employs the *bent* and *puff* models, any other column and VATD model could be used, and the statistical calculations appropriately adapted. Indeed, the framework introduced here provides an approach for developing maps for many hazard scenarios, assuming the cost of simulations is not prohibitive.

The structure of this paper is as follows. The numerical model of eruption column and VATD is explained in Section 2. Section 3 defines the overall approach to probabilistic model forecasting, with subsections detailing the calculation of probabilities from model ensembles and the procedure for minimum variance based source estimation. Section 5 describes the core computational challenges in the evaluation of expectation integrals, and our CUT approach to overcome these challenges. All these strands are brought together in Section 5, where a probabilistic forecast and hazard map is created and volcano source parameters estimated, using data from the 2010 Eyjafjallajökull volcano eruption. A discussion of results is presented in Section 6.

## 2. Volcanic plume model

Ash transport models can be divided into two broad categories: those intended to calculate eruption column and tephra fall deposit characteristics based on source vent conditions (eruption column model), as in Carey and Sparks [29], and those

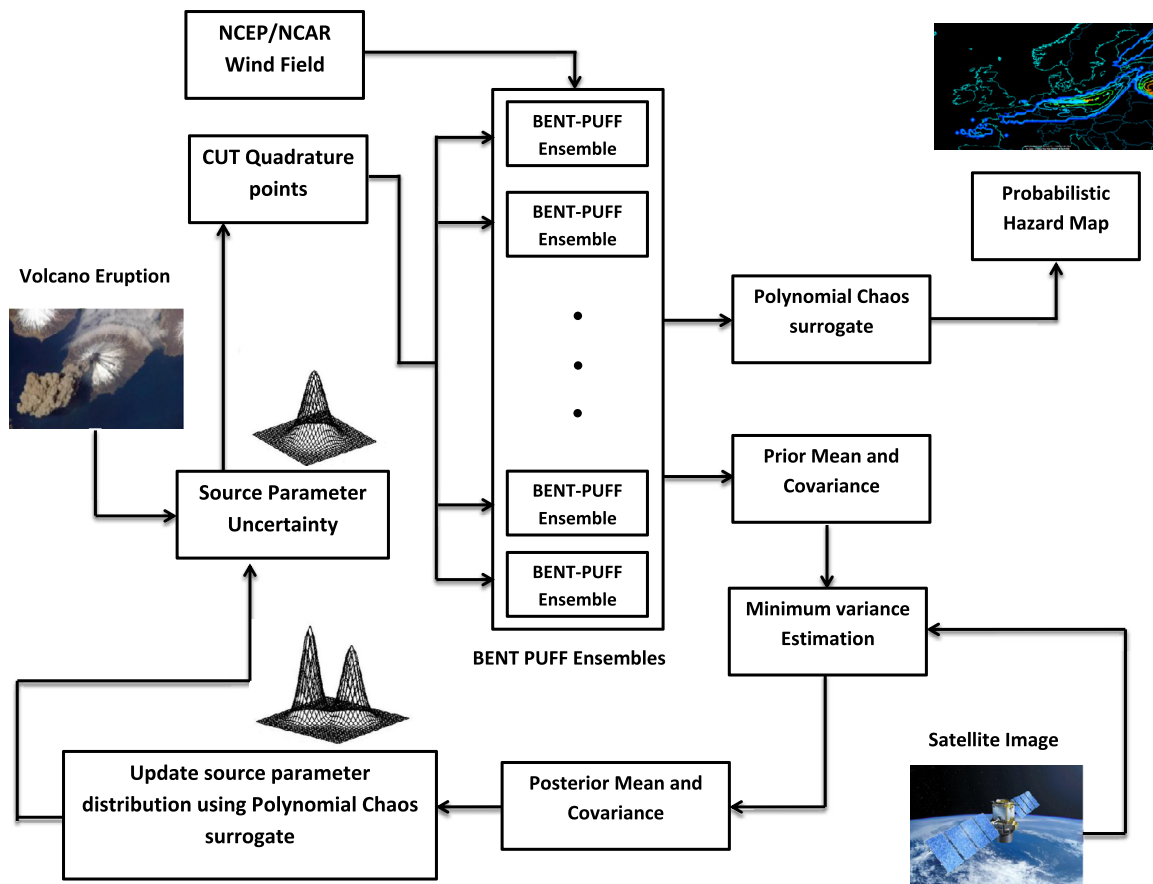


**Fig. 1.** Schematic view of probabilistic model forecast and source parameter estimation process while incorporating prior knowledge of source uncertainty and satellite imagery.

intended to forecast long-range atmospheric transport, dispersion and fallout (VATD model), as in Suzuki [30]. All ash transport models rely on the existence of an explicit relationship between the eruption column and atmospheric dynamics, and the resulting transport, dispersion and settling of the ash. The focus of this work is on the long-range movement of ash clouds, and not eruption column dynamics or tephra deposition. Therefore, a simple VATD model, but one that nonetheless contains several sources of uncertainty, is considered to focus attention on long-range transport and dispersion. Tanaka [31] and Searcy et al. [32] developed *puff*, an ash tracking model for forecasting the paths of incipient volcanic clouds. *puff* simplifies the eruption plume to a vertical source, and uses a Lagrangian pseudo-particle representation of the ash plume in a detailed 3-D regional windfield to determine the trajectory of the cloud. *puff* and other dispersion models have proven extremely useful in modeling the distal transport of ash for aviation safety [32]. During an eruption crisis, *puff* forecasts have been used to forecast ash cloud movement critical to the assessment of potential impacts – for example, on aircraft flight paths. *puff* has been validated against historic volcanic eruptions such as the 1992 Crater Peak vent eruption at Mount Spurr and the 2006 eruption at Mount Augustine with reasonable success [32,33]. To start a simulation, *puff* requires as inputs the eruption start time and duration, the initial plume height, the vertical distribution of particles of varying size, a representative wind field, and the simulation end time. At first, some of these parameters must be assumed, based on past activity of the volcano, or by using the Eruption Source Parameters (ESP) of Mastin et al. [34].

To initialize a *puff* simulation a collection of particles of different sizes must be specified as a function of altitude, a process that is not well constrained; see [35,36]. It is important to remember that *puff* particles are not simple surrogates for ash concentration, but are representatives of ejecta of a given size at a specified height. As such this number is a user-selected input that affects both simulation time and resolution of the output. In addition to particle grain-size distribution and windfield, other *puff* input parameters include the coefficient of turbulent diffusion, and particle settling speed, both of which are estimated. Instead of guessing the initial particle distribution as a function of height, a volcanic eruption plume model called *bent* is employed to provide initial conditions for the VATD model. The essential features of this coupling between *bent* and *puff* is described in [28]. *bent* solves the equations for mass, momentum and energy balance, averaged over a cross-sectional slice of the eruption column [37]. *bent* assumes a grain-size distribution of pyroclasts and, depending on the volcanic vent size and the speed of the ejecta, the model equations forecast the height distribution of the various sized clasts. *bent* has been tested against plume rise height data and ash dispersal data [36]. In particular, the discussion in that paper (among many others) corroborates that the scaling relationships derived in [38] between energy and plume rise height are valid for energetic volcanic plumes piercing the tropopause.



In a tool we call *bent-puff*, *bent* incorporates important physics of the volcano column and provides initial conditions for *puff*. On the one hand, physics guides the model coupling and determines how outputs from *bent* feed into *puff*. On the other hand, this coupling can be viewed as simply substituting one set of uncertain parameters in *puff* (vent size, velocity, clast size distribution) for an uncertain function of *bent* (particle height distribution). In any event, physically relevant inputs from the volcano source – together with their variability – are modeled and propagated through *bent* and *puff*.

### 3. Probabilistic hazard map

The problem of generating hazard maps corresponds to computing the probability of quantity of interest (QOI), such as the amount of ash present in the atmosphere at a given geographical location, given the probability distribution for model input parameters (hereafter when we speak of the model input parameters, we mean volcanic vent size, particle velocity at the vent, and grain size distribution). The accurate computation of probabilistic hazard map requires two principal actions:

1. The forward propagation of variability in model input parameters, in order to compute the probability of the QOI at a specified place and time;
2. The refinement of estimates of the model parameters by fusing remote-sensing observations of the ash cloud with the model forecast.

#### 3.1. Computing the probability of a QOI

A simplistic approach to computing hazard maps entails running ensembles of numerical simulations with a range of input values, and computing the relative frequency of a QOI. Unfortunately, a large number of realizations (perhaps  $\mathcal{O}(10^6)$ ) are generally required to get a good convergence in probability for the QOI. This computational load renders this simplistic approach impractical for many dynamic models. Instead one needs a more judiciously chosen method for computing probabilities, recognizing the potential for a trade-off between computational efficiency and the accuracy of probability computations.

In this work, we follow an approach outlined in Dalbey et al. [39] in which the gPC methodology was employed to create a fast, computationally cheap *polynomial surrogate model*, which is used to evaluate a large number of samples at minimal computational cost. In the standard gPC methodology, Galerkin collocation is used to generate a system of deterministic differential equations for the expansion coefficients. The Galerkin collocation step fails when applied to problems with non-polynomial nonlinearities, and can produce non-physical solutions when applied to hyperbolic equations. Non-intrusive spectral projection (NISP) or stochastic collocation methods can overcome these difficulties [40–42]. A different formulation of the NISP idea [39] known as polynomial chaos quadrature (PCQ) is used here. PCQ replaces the projection step of NISP with numerical quadrature. Thus our approach for computing the probability for a QOI involves (1) computing coefficients of the polynomial surrogate model according to the PCQ formulation; (2) sampling the surrogate at a large number of inputs at minimal computational cost. Let us describe this approach in more detail.

Let  $\mathbf{x}(t, \boldsymbol{\theta}) \in \mathbb{R}^n$  represent a vector of  $n$  quantities of interest which is a function of the uncertain model parameter vector  $\boldsymbol{\theta} = [\theta_1, \theta_2, \dots, \theta_m]^T \in \mathbb{R}^m$ . For example, the vector  $\mathbf{x}$  might represent the height at the top of an ash cloud and/or the ash concentration, at a specified 2D or 3D location, and the parameter vector  $\boldsymbol{\theta}$  might contain volcano source parameters (vent size, particle velocity at the vent, and grain size distribution).  $\boldsymbol{\theta}$  is assumed to be time invariant, and a function of a standardized random vector  $\boldsymbol{\xi} = [\xi_1, \xi_2, \dots, \xi_m]^T \in \mathbb{R}^m$  defined by a pdf  $p(\boldsymbol{\xi})$  with support  $\Omega$ . For example, the uncertain model parameter vector for *bent-puff*,  $\boldsymbol{\theta}$  consisting of volcano source parameters (vent size, particle velocity at the vent, mean grain size and standard deviation of grain size) can be assumed to be a uniformly distributed random vector which lies in the range:

$$\mathbf{a} \leq \boldsymbol{\theta} \leq \mathbf{b} \quad (1)$$

Hence,  $\boldsymbol{\theta}$  can be written as a function of  $\boldsymbol{\xi}$  consisting of four standardized uniform random variables between  $-1$  and  $1$ :

$$\theta_j = \frac{a_j + b_j}{2} + \frac{b_j - a_j}{2} \xi_j, \quad j = 1, 2, \dots, 4 \quad (2)$$

If  $\boldsymbol{\theta}$  is assumed to be Gaussian random vector with prescribed mean and covariance matrix, then  $\boldsymbol{\xi}$  can be a vector of Gaussian random variables with zero mean and identity covariance. Note that  $\boldsymbol{\theta}$  is not restricted to have uniform or Gaussian distribution. Ideally, it can have any prescribed distribution. Now, the QOI (say ash top-height at a geolocation) can be approximated as a linear combination of  $N$  polynomial functions of  $\boldsymbol{\xi}$ :

$$x_i(t, \boldsymbol{\theta}) = \sum_{k=0}^N x_{i_k}(t) \phi_k(\boldsymbol{\xi}) \quad (3)$$

where,  $\phi_k(\boldsymbol{\xi})$  are orthogonal polynomial basis function set with respect to  $p(\boldsymbol{\xi})$ . One can use the Gram–Schmidt orthogonalization to compute these basis functions.

In general, according to the PCQ methodology, the uncertain QOI,  $\mathbf{x}(t, \boldsymbol{\theta})$  and model parameter  $\boldsymbol{\theta}$  can be written as a linear combination of orthogonal polynomial basis functions,  $\phi_k(\boldsymbol{\xi})$ , which span the space of random variables  $\boldsymbol{\xi} = [\xi_1, \dots, \xi_m]^T$  and results in following polynomial surrogate model:

$$x_i(t, \boldsymbol{\theta}) = \sum_{k=0}^N x_{i_k}(t) \phi_k(\boldsymbol{\xi}) = \mathbf{x}_i^T(t) \boldsymbol{\Phi}(\boldsymbol{\xi}) \Rightarrow \mathbf{x}(t, \boldsymbol{\xi}) = \mathbf{X}_{pc}(t) \boldsymbol{\Phi}(\boldsymbol{\xi}), \quad i = 1, 2, \dots, n \quad (4)$$

$$\theta_j(\boldsymbol{\xi}) = \sum_{k=0}^N \theta_{j_k} \phi_k(\boldsymbol{\xi}) = \boldsymbol{\theta}_j^T \boldsymbol{\Phi}(\boldsymbol{\xi}) \Rightarrow \boldsymbol{\theta}(t, \boldsymbol{\xi}) = \boldsymbol{\theta}_{pc} \boldsymbol{\Phi}(\boldsymbol{\xi}), \quad j = 1, 2, \dots, m \quad (5)$$

Here  $\mathbf{X}_{pc}$  and  $\boldsymbol{\theta}_{pc}$  are matrices composed of coefficients of the PC expansion for  $\mathbf{x}$  and  $\boldsymbol{\theta}$ . The coefficients  $\theta_{i_k}$  are obtained by making use of the *normal equation*:

$$\theta_{i_k} = \frac{\mathbb{E}[\theta_i(\boldsymbol{\xi}) \phi_k(\boldsymbol{\xi})]}{\mathbb{E}[\phi_k(\boldsymbol{\xi}) \phi_k(\boldsymbol{\xi})]} \quad (6)$$

In this expression, the expected value of a sufficiently smooth function  $u(\boldsymbol{\xi})$  is defined as:

$$\mathbb{E}[u(\boldsymbol{\xi})] = \int u(\boldsymbol{\xi}) p(\boldsymbol{\xi}) d\boldsymbol{\xi} \quad (7)$$

Similarly, the coefficients of  $x_{i_k}$ 's can be found from:

$$x_{i_k} = \frac{\mathbb{E}[x_i(t, \boldsymbol{\theta}(\boldsymbol{\xi})) \phi_k(\boldsymbol{\xi})]}{\mathbb{E}[\phi_k(\boldsymbol{\xi}) \phi_k(\boldsymbol{\xi})]} \quad (8)$$

In our calculations, numerical quadrature replaces exact integration. Specifically, the integrals in Eq. (6) and Eq. (8) can be written as:

$$\mathbb{E}[\phi_i(\boldsymbol{\xi}) \phi_j(\boldsymbol{\xi})] = \int \phi_i(\boldsymbol{\xi}) \phi_j(\boldsymbol{\xi}) p(\boldsymbol{\xi}) d\boldsymbol{\xi} \simeq \sum_{q=1}^M w_q \phi_i(\boldsymbol{\xi}^q) \phi_j(\boldsymbol{\xi}^q) \quad (9)$$

$$\mathbb{E}[x_i(t, \boldsymbol{\theta}(\boldsymbol{\xi})) \phi_j(\boldsymbol{\xi})] = \int x_i(t, \boldsymbol{\theta}(\boldsymbol{\xi})) \phi_j(\boldsymbol{\xi}) p(\boldsymbol{\xi}) d\boldsymbol{\xi} \simeq \sum_{q=1}^M w_q x_i(t, \boldsymbol{\xi}^q) \phi_j(\boldsymbol{\xi}^q) \quad (10)$$

$$\mathbb{E}[\theta_i(\boldsymbol{\xi}) \phi_j(\boldsymbol{\xi})] = \int \theta_i(\boldsymbol{\xi}) \phi_j(\boldsymbol{\xi}) p(\boldsymbol{\xi}) d\boldsymbol{\xi} \simeq \sum_{q=1}^M w_q \theta_i(\boldsymbol{\xi}^q) \phi_j(\boldsymbol{\xi}^q) \quad (11)$$

Notice that  $x_i(t, \boldsymbol{\xi}^q)$  represent the quantity of interest at time  $t$  with model parameter vector being evaluated at  $\boldsymbol{\xi}^q$ , where  $\boldsymbol{\xi}^q$  corresponds to quadrature value of parameter vector  $\boldsymbol{\xi}$ . That is, the VATD model is solved for each input parameter vector  $\boldsymbol{\xi}^q$ , and the QOI is then computed from these simulations. The resulting method can be viewed as a “smart” MC-like evaluation of the model equations, with sample points selected by quadrature rules. However instead of performing intensive simulations, the polynomial surrogate model Eq. (4) can be substituted in order to calculate the probability of the QOI at a given location.

To summarize, then, given a specific location, the following algorithm can be used to compute a hazard map for a QOI:

- Step 1: In the space of random variables, generate sampling points as combinations of input parameters, treated as random variables, corresponding to the selected quadrature scheme;
- Step 2: Perform a simulation at each sample point using the VATD model to generate a map of the QOI, as a function of position;
- Step 3: Use Eq. (8) to compute the PC expansion coefficients corresponding to the QOI, for each location;
- Step 4: Choose a large set of secondary sample points in the stochastic space, generated from the probability density function  $p(\boldsymbol{\xi})$ ;
- Step 5: Compute the QOI for each secondary sample point from the surrogate model.  
add here:
- Step 6: Find the fraction of secondary sample points for which QOI is greater than the prescribed threshold. This fraction is an estimate of probability (hazard map) of the QOI to be greater than the prescribed threshold.

### 3.2. Computing posterior distribution of model parameters

Of course using any sensor data that might become available to correct and refine the model forecast will reduce the uncertainty and will improve the accuracy of the generated hazard map. Given a forecast of the QOI  $\mathbf{x}_k$ , standard Bayesian algorithms assume a measurement model  $\mathbf{h}$  to obtain the measurement  $\mathbf{y}_k$ :

$$\mathbf{y}_k \triangleq \mathbf{y}(t_k) = \mathbf{h}(\mathbf{x}_k, \boldsymbol{\theta}) + \mathbf{v}_k \quad (12)$$

where the nonlinear function  $\mathbf{h}(\cdot)$  captures the sensor model and  $\mathbf{v}_k$  is the measurement noise with a correlation matrix  $\mathbf{R}$ . The key challenge is to find an estimate for the parameter  $\boldsymbol{\theta}$  and its associated uncertainty bounds, given some measurement data. A schematic representation of the estimation process is shown in Fig. 1.

As discussed in Section 1, various approaches exist to address this stochastic inverse problem. Many of these approaches are either computationally expensive, or restricted to a specific type of dynamical systems. Here we employ a linear unbiased minimum variance estimation method to minimize the trace of the posterior parameter covariance matrix:

$$J = \min_{\boldsymbol{\theta}} \text{Tr}[\mathbb{E}[(\boldsymbol{\theta} - \mathbb{E}[\boldsymbol{\theta}])(\boldsymbol{\theta} - \mathbb{E}[\boldsymbol{\theta}])^T]] \quad (13)$$

It should be noted that the minimum variance formulation is valid for any pdf, although the formulation makes use of only the mean and covariance information. It provides the maximum a-posteriori estimate when model dynamics and measurement model is linear and state uncertainty is Gaussian. Minimizing the cost function  $J$  subject to the constraint of being an unbiased estimate, and using linear updating, allows us to compute the first two moments of the posterior distribution [25,43]:

$$\hat{\boldsymbol{\theta}}_k^+ = \hat{\boldsymbol{\theta}}_k^- + \mathbf{K}_k[\mathbf{y}_k - \mathbb{E}^-[ \mathbf{h}(\mathbf{x}_k, \boldsymbol{\theta}) ]]$$

$$\boldsymbol{\Sigma}_k^+ = \boldsymbol{\Sigma}_k^- + \mathbf{K}_k \boldsymbol{\Sigma}_{\theta y} \quad (15)$$

In this update, the gain matrix  $\mathbf{K}$  is given by

$$\mathbf{K}_k = \boldsymbol{\Sigma}_{\theta y}^T (\boldsymbol{\Sigma}_{hh}^- + \mathbf{R}_k + \mathbf{Q}_k)^{-1} \quad (16)$$

Here,  $\hat{\boldsymbol{\theta}}_k^-$  represents the prior mean for the parameter vector  $\boldsymbol{\theta}$  while incorporating measurements up to time interval  $t_{k-1}$  and  $\hat{\boldsymbol{\theta}}_k^+$  represents the posterior mean for parameter vector  $\boldsymbol{\theta}$  while incorporating measurements up to time interval  $t_k$ :

$$\hat{\boldsymbol{\theta}}_k^- \triangleq \mathbb{E}^-[ \boldsymbol{\theta}_k ] = \int_{\xi} \boldsymbol{\theta}_k^-(\xi) p(\xi) d\xi \quad (17)$$

$$\hat{\boldsymbol{\theta}}_k^+ \triangleq \mathbb{E}^+[ \boldsymbol{\theta}_k ] = \int_{\xi} \boldsymbol{\theta}_k^+(\xi) p(\xi) d\xi \quad (18)$$

Similarly, the prior and posterior covariance matrices  $\boldsymbol{\Sigma}_k^-$  and  $\boldsymbol{\Sigma}_k^+$  can be written as:

$$\boldsymbol{\Sigma}_k^- \triangleq \mathbb{E}^-[ (\boldsymbol{\theta}_k - \hat{\boldsymbol{\theta}}_k^-)(\boldsymbol{\theta}_k - \hat{\boldsymbol{\theta}}_k^-)^T ] = \int_{\xi} (\boldsymbol{\theta}_k^-(\xi) - \hat{\boldsymbol{\theta}}_k^-)(\boldsymbol{\theta}_k^-(\xi) - \hat{\boldsymbol{\theta}}_k^-)^T p(\xi) d\xi \in \mathbb{R}^{m \times m} \quad (19)$$

$$\boldsymbol{\Sigma}_k^+ \triangleq \mathbb{E}^+[ (\boldsymbol{\theta}_k - \hat{\boldsymbol{\theta}}_k^+)(\boldsymbol{\theta}_k - \hat{\boldsymbol{\theta}}_k^+)^T ] = \int_{\xi} (\boldsymbol{\theta}_k^+(\xi) - \hat{\boldsymbol{\theta}}_k^+)(\boldsymbol{\theta}_k^+(\xi) - \hat{\boldsymbol{\theta}}_k^+)^T p(\xi) d\xi \in \mathbb{R}^{m \times m} \quad (20)$$

Also,  $\mathbf{Q}_k$  denotes the model error covariance matrix in Eq. (16) which encapsulates the model's inaccuracies. The matrices  $\boldsymbol{\Sigma}_{\theta y}$  and  $\boldsymbol{\Sigma}_{hh}$  are defined as:

$$\hat{\mathbf{h}}_k^- \triangleq \mathbb{E}^-[ \mathbf{h}(\mathbf{x}_k, \boldsymbol{\theta}) ] = \int_{\xi} \underbrace{\mathbf{h}(\mathbf{x}_k^-(\xi), \boldsymbol{\theta}^-(\xi))}_{\mathbf{h}_k} p(\xi) d\xi \quad (21)$$

$$\boldsymbol{\Sigma}_{\theta y} \triangleq \mathbb{E}^-[ (\boldsymbol{\theta} - \hat{\boldsymbol{\theta}}_k^-)(\mathbf{h}_k - \hat{\mathbf{h}}_k^-)^T ] = \int_{\xi} (\boldsymbol{\theta}^-(\xi) - \hat{\boldsymbol{\theta}}_k^-)(\mathbf{h}_k - \hat{\mathbf{h}}_k^-)^T p(\xi) d\xi \quad (22)$$

$$\boldsymbol{\Sigma}_{hh}^- \triangleq \mathbb{E}^-[ (\mathbf{h}_k - \hat{\mathbf{h}}_k^-)(\mathbf{h}_k - \hat{\mathbf{h}}_k^-)^T ] = \int_{\xi} (\mathbf{h}_k - \hat{\mathbf{h}}_k^-)(\mathbf{h}_k - \hat{\mathbf{h}}_k^-)^T p(\xi) d\xi \quad (23)$$

Here again, the expectation integrals in Eq. (21), Eq. (22), and Eq. (23) can be computed by suitable quadrature rules:

$$\hat{\mathbf{h}}_k^- \triangleq \mathbb{E}^-[ \mathbf{h}(\mathbf{x}_k, \boldsymbol{\theta}) ] \simeq \sum_{q=1}^M w_q \underbrace{\mathbf{h}(\mathbf{x}_k(\xi^q), \boldsymbol{\theta}(\xi^q))}_{\mathbf{h}_q} \quad (24)$$

$$\boldsymbol{\Sigma}_{\theta y} \triangleq \mathbb{E}^-[ (\boldsymbol{\theta}_k - \hat{\boldsymbol{\theta}}_k^-)(\mathbf{h}_k - \hat{\mathbf{h}}_k^-)^T ] \simeq \sum_{q=1}^M w_q (\boldsymbol{\theta}_k(\xi^q) - \hat{\boldsymbol{\theta}}_k^-)(\mathbf{h}_q - \hat{\mathbf{h}}_k^-)^T \quad (25)$$



$$\Sigma_{hh}^- \triangleq \mathbb{E}^-[(\mathbf{h}(\mathbf{x}_k) - \hat{\mathbf{h}}_k^-)(\mathbf{h}(\mathbf{x}_k) - \hat{\mathbf{h}}_k^-)^T] \simeq \sum_{q=1}^M w_q (\mathbf{h}_q - \hat{\mathbf{h}}_k^-)(\mathbf{h}_q - \hat{\mathbf{h}}_k^-)^T \quad (26)$$

Again we point out that  $\mathbf{h}_q$  represents computational measurements corresponding to simulation runs with input parameter determined by  $\xi^q$ . Furthermore, one can update the polynomial expansion coefficients of Eq. (5) at the time measurement data becomes available, as described in Ref. [25]. More specifically, the posterior expected value of  $\boldsymbol{\theta}$  at a specific time step  $k$  can be written in terms of the PC expansion coefficients:

$$\hat{\boldsymbol{\theta}}_k^+ \triangleq \mathbb{E}^+[\boldsymbol{\theta}_k] = [\boldsymbol{\theta}_{pc_1}^+] \quad (27)$$

where,  $\boldsymbol{\theta}_{pc_1}^+$  is the posterior value of the first column of the matrix  $\boldsymbol{\theta}_{pc}$ . Similarly, assuming orthonormality of basis functions  $\phi_i(\xi)$ 's, the posterior covariance matrix of  $\boldsymbol{\theta}$  can be written as:

$$\Sigma_k^+ \triangleq \mathbb{E}^+[(\boldsymbol{\theta}_k - \hat{\boldsymbol{\theta}}_k^+)(\boldsymbol{\theta}_k - \hat{\boldsymbol{\theta}}_k^+)^T] \in \mathbb{R}^{m \times m}, \quad \Sigma_k^+(i, j) = \sum_{l=1}^N \theta_{il}^+ \theta_{jl}^+, \quad i, j = 1, \dots, m \quad (28)$$

where,  $\theta_{il}^+$  is the posterior value of  $l$ th coefficient in the PC expansion of  $\theta_i$ . Now, by combining Eq. (27) and Eq. (28) with Eq. (14) and Eq. (15), we find

$$\boldsymbol{\theta}_{pc_1}^+(i) = \hat{\boldsymbol{\theta}}_k^+(i), \quad i = 1, 2, \dots, m \quad (29)$$

$$\sum_{l=1}^N \theta_{il}^+ \theta_{jl}^+ = \Sigma_k^+(i, j), \quad i, j = 1, \dots, m \quad (30)$$

Eq. (29) provides values of the components of  $\boldsymbol{\theta}_{pc_1}^+$ , and Eq. (30) provides  $m^2$  equations for the remaining  $mN$  unknown coefficients. Depending on the order of the PC expansion and the dimension of  $\boldsymbol{\theta}$ , the resulting equations can be over-determined, properly determined, or under-determined. Different approaches must be used to solve Eq. (30), depending on the character of the matrix.

#### 4. Computation challenges

Accurate evaluation of the various expectation integrals defined in the previous section is a crucial task to compute accurate hazard maps. Several quadrature schemes exist in the literature to evaluate integrals, the most popular being Gaussian Quadrature Rules [27]. The Gaussian quadrature scheme involves deterministic points carefully selected to reproduce exactly the value of integrals of polynomials of given order. According to Gaussian quadrature, for 1-dimensional integrals one requires  $M$  quadrature points to exactly reproduce the integral of a polynomial of degree  $2M - 1$ . In  $m$ -dimension space, common practice is to take the tensor product of 1-dimensional quadrature points, yielding  $M^m$  quadrature points. Even for a moderate-dimension system involving, say, 6 random variables, the number of points required to evaluate the expectation integral with only 5 points along each direction is  $5^6 = 15,625$ . This is a non-trivial number of points that might make the calculation of an integral computationally expensive, especially when the evaluation of the integrand at each point is, itself, an expensive procedure. The sparse grid quadratures, and in particular Smolyak quadrature, take the sparse product of one dimensional quadrature rules and thus have fewer points than the equivalent Gaussian quadrature rules, but at the cost of introducing negative weights, [26,44]. Fortunately, the Gaussian quadrature rule is not minimal for  $m \geq 2$ , and there exists quadrature rules requiring fewer points in high dimensions [27].

##### 4.1. Conjugate Unscented Transform

Recently, Adurthi et al. [5] have proposed non-product quadrature rules based on the Conjugate Unscented Transformation (CUT), which computes multi-dimension expectation integrals involving Gaussian and uniform pdf by constraining the evaluation points to lie on specially defined axes. These new sets of so-called sigma points are guaranteed to exactly evaluate expectation integrals involving polynomial functions with significantly fewer points. We summarize the CUT methodology now, and refer the reader to [4–7] and Appendix A for further details.

The CUT approach can be considered an extension of the conventional Unscented Transformation method that satisfies additional, higher order moment constraints. Rather than using tensor products as in Gauss quadrature, the CUT approach judiciously selects specific structures to extract *symmetric* quadrature points. Like Gauss quadrature, this process is designed to exactly integrate polynomials of total degree  $2M - 1$  in  $m$ -dimensional space, with fewer than  $M^m$  points.

To illustrate the CUT approach, consider the problem of approximating the expected value of a function  $f(\mathbf{x})$ :

$$\mathbb{E}[f(\mathbf{x})] = \int_{\Omega} f(\mathbf{x}) p(\mathbf{x}) d\mathbf{x} \simeq \sum_{i=1}^n w_i f(\mathbf{x}_{(i)}) \quad (31)$$

**Table 1**  
Different types of CUT points defined in  $N$ -dimensional space.

Type	Sample point	Number of points
$\sigma$	$(1, 0, 0, \dots, 0)$	$2N$
$c^M$	$(\underbrace{1, 1, \dots, 1}_M, \underbrace{0, 0, \dots, 0}_{N-M})$	$2^M \binom{N}{M}$
$s^N(h)$	$(h, 1, 1, \dots, 1)$	$N2^N$

where,  $\mathbf{x} = [x_1, x_2, \dots, x_m]^T \in \mathbb{R}^m$  and  $p(\mathbf{x})$  is either the uniform or Gaussian density function defined over the domain  $\Omega \subset \mathbb{R}^N$ . Denote the cubature points as  $\mathbf{x}_{(i)} \in \Omega$ , and  $w_i > 0$  as the corresponding scalar weights. Assuming that  $f(\mathbf{x})$  has a valid Maclaurin series given by

$$f(\mathbf{x}) = \sum_{n_1=0}^{\infty} \sum_{n_2=0}^{\infty} \dots \sum_{n_m=0}^{\infty} \frac{x_1^{n_1} x_2^{n_2} \dots x_m^{n_m}}{n_1! n_2! \dots n_m!} \frac{\partial^{n_1+n_2+\dots+n_m} f}{\partial^{n_1} x_1 \partial^{n_2} x_2 \dots \partial^{n_m} x_m} \quad (32)$$

the expectation of  $f(\mathbf{x})$  can be written as:

$$\mathbb{E}[f(\mathbf{x})] = \sum_{n_1=0}^{\infty} \sum_{n_2=0}^{\infty} \dots \sum_{n_m=0}^{\infty} \frac{\mathbb{E}[x_1^{n_1} x_2^{n_2} \dots x_m^{n_m}]}{n_1! n_2! \dots n_m!} \frac{\partial^{n_1+n_2+\dots+n_m} f}{\partial^{n_1} x_1 \partial^{n_2} x_2 \dots \partial^{n_m} x_m} \quad (33)$$

Thus the problem of evaluating the expected value of  $f(\mathbf{x})$  is reduced to computing higher order moments of random vector  $\mathbf{x}$  distributed according to the pdf  $p(\mathbf{x})$ . Substitution of Eq. (32) into Eq. (31) leads to the expression

$$\sum_{i=1}^n w_i f(\mathbf{x}_{(i)}) = \sum_{n_1=0}^{\infty} \sum_{n_2=0}^{\infty} \dots \sum_{n_m=0}^{\infty} \frac{(\sum_{i=1}^n w_i \prod_{k=1}^m x_{(i,k)}^{n_k})}{n_1! n_2! \dots n_m!} \frac{\partial^{n_1+n_2+\dots+n_m} f(\mathbf{0})}{\partial^{n_1} x_1 \partial^{n_2} x_2 \dots \partial^{n_m} x_m} \quad (34)$$

Comparing Eq. (34) and Eq. (33) results in a set of algebraic equations known as *Moment Constraint Equations*:

$$\mathbb{E}[x_1^{n_1} x_2^{n_2} \dots x_N^{n_N}] = \sum_{i=1}^n w_i \prod_{k=1}^m x_{(i,k)}^{n_k} \quad (35)$$

Notice that the left hand side of this equation contains the moments of the input parameter density function, and the right hand side is a function of the unknown position of quadrature points. The CUT methodology involves finding quadrature points that satisfy Eq. (35) up to a desired order of moments. Assuming  $p(\mathbf{x})$  to be symmetric, the cubature points are chosen to lie symmetrically about appropriately defined directions:

- *Principal axes*: Generally in an  $m$ -dimensional Cartesian space, there are  $m$  orthogonal coordinate axes centered at the origin which correspond to eigenvectors of the covariance of the input random variable. These axes are called *principal axes* which are denoted by  $\sigma$ . The corresponding point on these axes are shown as  $\sigma_j$ ,  $j = 1, 2, \dots, 2m$ .
- *Conjugate axes*: Conjugate axes, denoted by  $c^P$  ( $P \leq m$ ), are the axes constructed from all the combinations and sign permutations of the set of principal axes taken  $P$  at a time. These points are shown by  $c_i^P$ , where  $i = 1, 2, \dots, 2^P \binom{m}{P}$ .
- *Scaled conjugate axes*: The remainder of the cubature points are found from the  $m$ th scaled conjugate axes, which are constructed from all the combinations with sign permutations of the set of principal axes such that in every combination exactly one principal axis is scaled by a scaling parameter  $h$ . These set of axes are labeled as  $s^m(h)$ , and the points are listed as  $s_i^m(h)$  where  $i = 1, 2, \dots, m2^m$ .

Table 1 presents one sample point on each of these directions in  $m$  dimensions. A schematic view of these points in 3 dimensional space is given in Fig. 2.

The next step is to select combinations of the points just defined. All the selected points that lie on the same set of symmetric axes should be equidistant from the origin and should have equal weights. For each selected point, two unknown variables, a weight  $w_i$  and a scaling parameter  $r_i$  are assigned. The moment constraints equations for the desired order are derived in terms of unknown variables  $r_i$  and  $w_i$ . Because of the symmetries of cubature points, the odd-order moment constraints equations are automatically satisfied, so the  $w_i$  and  $r_i$  are found by solving just the even order equations. Notice that different sets of cubature points can be found, depending on  $m$  and the order of the moment constraint equations. Appendix A employs the CUT procedure to compute 8th order quadrature points in 4-dimensional space; the interested reader may consult [4,5] for other illustrations.

The CUT quadrature approach uses just a small number of points, relative to Gauss quadrature, to compute an integral with the same accuracy. Fig. 3 represents the number of quadrature points required, for 8th order accuracy, by different quadrature schemes (CUT, Gauss–Legendre, Clenshaw–Curtis and Sparse Grid), for a uniform random variable, as a function of the dimensionality of the random variable. From this figure, it is clear that the growth in the number of quadrature points

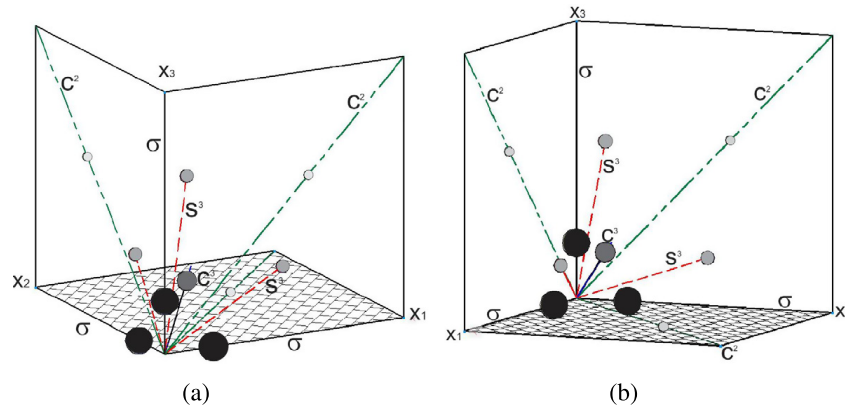


Fig. 2. Different types of cubature points in 3 dimensional Cartesian space in different views.

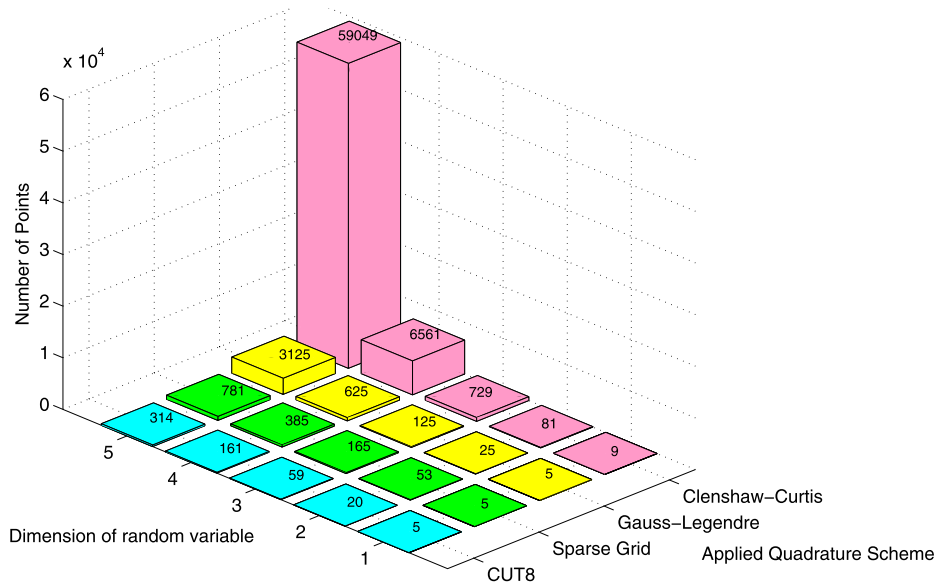


Fig. 3. Comparison of number of 8th order quadrature points required for different quadrature schemes, as a function of the dimension of the random variable.

with dimension is much smaller for the CUT method, especially compared to the Gauss-Legendre and Clenshaw-Curtis approaches. The CUT method requires fewer than half the number of quadrature points as the sparse grid Smolyak approach. As one specific example, 161 CUT quadrature points are required to satisfy 8th order moments in 4-dimensional space, but 6561 points are required for Clenshaw-Curtis quadrature, 625 for Gauss-Legendre quadrature, and 385 for sparse grid quadrature.

#### 4.2. Other challenges

One other computational challenge can arise in the parameter estimation, namely operations with a large and perhaps poorly conditioned Kalman Gain matrix  $\mathbf{K}_k$  in Eq. (16). To perform the necessary linear algebra operations, we use the state-of-the-art PETSc solver [45] together with good preconditioning. Block Jacobi and Additive Schwarz preconditioning were used here. Performance of the two preconditioners was comparable in terms of numbers of iterations required to obtain a specified residual, so we chose to use the less computationally expensive block Jacobi method for our test problem. Of course for different problems, other preconditioners might prove better. In general, matrix inversion is very sensitive to faulty data or other spurious artifacts, and steps should be taken to remove bad data whenever possible. Care should be exercised when data is suspect, to preclude erroneous forecasts.

### 5. Numerical experiments

The performance of the proposed methodology for generating accurate hazard maps and for updating model parameter estimates, is assessed using data from the April 2010 Eyjafjallajökull eruption in Iceland. The bent volcanic column model is used to generate initial ash cloud data for the puff VATD model [32], based on the Eyjafjallajökull eruption over the time period 14–16 April 2010. bent produces mass loading, plume height, and grain size distribution, which is used in

**Table 2**

Eruption source parameters based on observations of Eyjafjallajökull volcano and information from other similar eruptions of the past.

Parameter	Value range	PDF	Comment
Vent radius, $b_0$ , (m)	65–150	Uniform, + definite	Measured from IMO radar image of summit vents on 14 April 2010
Vent velocity, $w_0$ , (m/s)	45–124	Uniform, + definite	Measured by infrasound [50] 6–21 May, when MER similar to 14–18 April
Mean grain size, $Md_\phi$ , $\phi$	3.5–7	Uniform, $\in \mathbb{R}$	[51], Table 1, vulcanian and phreatoplinian. A. Hoskuldsson, Eyjafjallajökull Eruption Workshop, 09/2010, presentation, 'Vulcanian with unusual production of fine ash'.
$\sigma_\phi$ , $\phi$	0.5–3	Uniform, $\in \mathbb{R}$	[51], Table 1, vulcanian and phreatoplinian
Eruption temperature	1200 °C	Fixed	[28]
Erupted water mass fraction	0.017	Fixed	[28]
Eruption duration	3 hr	Fixed	[28]

**Table 3**Location 52N, 13.5E: conc is the puff computed absolute air concentration (in mg/m<sup>3</sup>) in a grid cell of size 0.5° × 0.5° × 2 km at 1200 hr on 16th April, 2010, and count is the number of puff particles in that cell.

Number of ash particles	height (m)	conc.	count	height	conc.	count	height	conc.	count
10 <sup>5</sup>	3000	$7.4 \times 10^{-5}$	28	5000	$4.23 \times 10^{-5}$	16	7000	–	–
$5 \times 10^5$	3000	$1.17 \times 10^{-4}$	221	5000	$3.54 \times 10^{-5}$	67	7000	–	–
10 <sup>6</sup>	3000	$1.12 \times 10^{-4}$	405	5000	$4.12 \times 10^{-5}$	156	7000	–	–
$2 \times 10^6$	3000	$1.12 \times 10^{-4}$	884	5000	$4.03 \times 10^{-5}$	305	7000	–	–
$4 \times 10^6$	3000	$1.09 \times 10^{-4}$	1655	5000	$4.10 \times 10^{-5}$	3620	7000	$1.32 \times 10^{-7}$	2
$8 \times 10^6$	3000	$1.15 \times 10^{-4}$	3471	5000	$4.15 \times 10^{-5}$	1256	7000	$1.98 \times 10^{-7}$	6
10 <sup>7</sup>	3000	$1.10 \times 10^{-4}$	4151	5000	$3.99 \times 10^{-5}$	1510	7000	$2.91 \times 10^{-7}$	11

puff, given atmospheric winds and volcanic source conditions. Icelandic Meteorological Office (IMO) Keflavik radiosonde data from 14 April 00Z, where 00Z refers to midnight in Universal Time, Z (near the initiation of the eruption) was used to generate the atmospheric winds for bent. puff, together with a given windfield, tracks the propagation of ash from Iceland to Europe. puff can be run using one of several numerical weather prediction (NWP) windfields [46–49]. These NWP models are available at different levels of spatial and temporal resolution. In this case, puff uses global NCEP/NCAR reanalysis wind fields to propagate ash, using 6-hr, 2.5° data. These wind fields assimilate observation wind data into model runs. Output from a deterministic puff model run consists simply of the position of the representative numerical particles; one can smooth this positions to determine a smoothed concentration field. The outputs are post-processed to extract other quantities of interest, such as maximum height of ash at a given geographical location. The top-height of ash is a useful quantity for the purpose of air traffic routing.

All four volcano source parameters – vent radius  $b_0$ , vent velocity  $w_0$ , mean grain size  $Md_\phi$ , and standard deviation of grain size  $\sigma_\phi$  – are assumed to be uncertain, and the prior density functions for these parameters, based upon previous eruption studies, are listed in Table 2. The CUT quadrature scheme described above was used to produce initial ensembles of source parameters. In earlier work [28], it was shown that an 8th order quadrature scheme is sufficient for computing statistics of ash top-height. From Section 4.1, 161 CUT quadrature points were generated. Following runs of bent corresponding to CUT quadrature points, each bent output was then propagated through puff, which was then run for three days. The outputs from puff were then used to create a polynomial surrogate model of degree 4 for ash top-height. 50,000 evaluations of ash top-height were evaluated using the surrogate, which were then used to compute the probabilistic hazard map described in Section 3.1.

Meteosat-9 retrievals of ash-cloud height were used to validate the probabilistic hazard map methodology and to refine prior probability density functions. Volcanic ash was identified in the satellite data using the methodology described in [52] and [53]. The ash loading (mass per unit area) and ash cloud height were retrieved using an optimal estimation approach [54,55]. The locations where satellite observed top-height is non-zero were used in the minimum variance estimation procedure to compute posterior mean and covariance for source parameters by making use of Eqs. (14)–(16). From computed posterior mean and covariance, the polynomial chaos coefficients for source parameters are updated and hence, corresponding density functions, making use of the procedure listed in Section 3.2.

### 5.1. Computing probability of ash top-height

Like any Lagrangian model, the accuracy of the bent-puff model is greatly influenced by the number of ash particles. To understand the convergence of the approach proposed here, it is necessary to understand how the number of ash particles impact the output of puff. For this purpose, probabilistic hazard maps were computed corresponding to five different values of the number of ash particles:  $4 \times 10^6$ ,  $10^7$ ,  $2 \times 10^7$ ,  $4 \times 10^7$ , and  $8 \times 10^7$ . For all puff runs, the vertical position of ash particles is quantized in 2-km altitude levels. Table 3 represents the absolute and relative ash concentration at a particular location, for different altitudes and different number of ash particles used in one deterministic run of bent-puff.

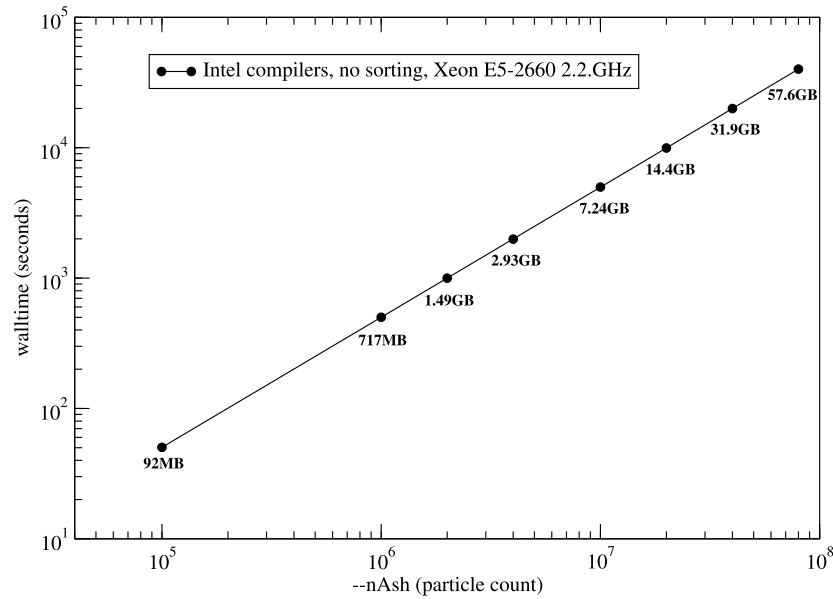


Fig. 4. Processor time for single deterministic run of bent-puff vs. number of ash particles.

As expected, both the concentration and the ash top-height are significantly affected by the number of ash particles. The table shows that, by increasing the number of ash particles from  $2 \times 10^6$  to  $4 \times 10^6$ , the maximum height of ash at location 52N, 13.5E increases from 5000 m to 7000 m. Fig. 4 shows the processor time and estimates of memory required to complete a single run of the bent-puff model, as a function of the number of particles. From this plot, it is clear that the computational time increases exponentially with an increase in number of ash particles in a run. Here again the trade-off between desired accuracy and computational cost is evident. These results are consistent with prior studies performed on the convergence of puff output [56].

Fig. 5 shows the probability of ash top-height being greater than or equal to specified threshold  $h_{thresh}$  for a few specific locations and times, as a function of the number of ash particles. It appears that the probability values have converged for lower value of  $h_{thresh}$ , but considerable fluctuations for  $h_{thresh} = 5000$  m and  $h_{thresh} = 7000$  m remain. This observation is consistent with the convergence of bent-puff model shown in Table 3. One surmises that these fluctuations can be attributed to the accuracy of the puff model rather than any aliasing error in the convergence of quadrature scheme.

Fig. 6 shows the probabilistic hazard map consisting of probability of ash top-height being greater than or equal to  $h_{thresh} = 3$  km for different numbers of ash particles in bent-puff model, overlaid with satellite observed ash top-height greater than or equal to 3 km, on April 16th, 0600 hrs (54 hours after eruption). Fig. 7 shows the probability of ash top-height to be greater than or equal to  $h_{thresh} = 5$  km, overlaid with satellite observed ash top-height greater than or equal to 5 km, again on April 16th, 0600 hrs. From these plots, one can conclude that the probabilistic hazard map calculations have converged with respect to number of ash particles used and satellite imagery consistently fall within most probable forecasted region.

Fig. 8 shows the probability map of ash top-height exceeding 1 km overlaid with satellite observed ash top-height at six-hour interval for 16th April. Most of the satellite data lies within the high probability region, although the probable ash cloud footprint is quite large, owing to the large uncertainty in prior source parameters. Note also the predicted ash in the north-east corner of the image is not supported by satellite imagery; further study indicates this area was obscured by meteorological clouds.

To compare the accuracy of the CUT quadrature scheme, the 8th order Clenshaw–Curtis (CC) quadrature scheme with  $9^4$  quadrature points is employed to compute probabilistic hazard maps. The convergence of the Clenshaw–Curtis quadrature scheme in computing the mean and standard deviation of the ash top-height has been studied in earlier work [28]. Fig. 9 shows the probability map of ash top-height exceeding 1 km overlaid with satellite observed ash top-height at six-hour intervals for 16th April. From Fig. 8 and Fig. 9, it is clear that probability maps computed with the help of CUT and CC quadrature schemes are indistinguishable. We conclude that the CUT methodology provides an order of magnitude computation savings without the loss of any accuracy.

## 5.2. Refining prior source parameters distribution

As just shown, due to the large uncertainty in source parameters, the uncertainty in the probable ash footprint is very high (see Fig. 8). This finding suggests we should re-compute the source parameter distributions making use of satellite observations. The procedure listed in Section 3.2 is used to compute posterior estimate for the source parameters and the corresponding probability density function, using satellite data from three different times (April 16th at 0600 hrs, 1200 hrs, and 1800 hrs). Satellite observed ash top-heights are estimated to be accurate to within 100 m intervals around the ob-



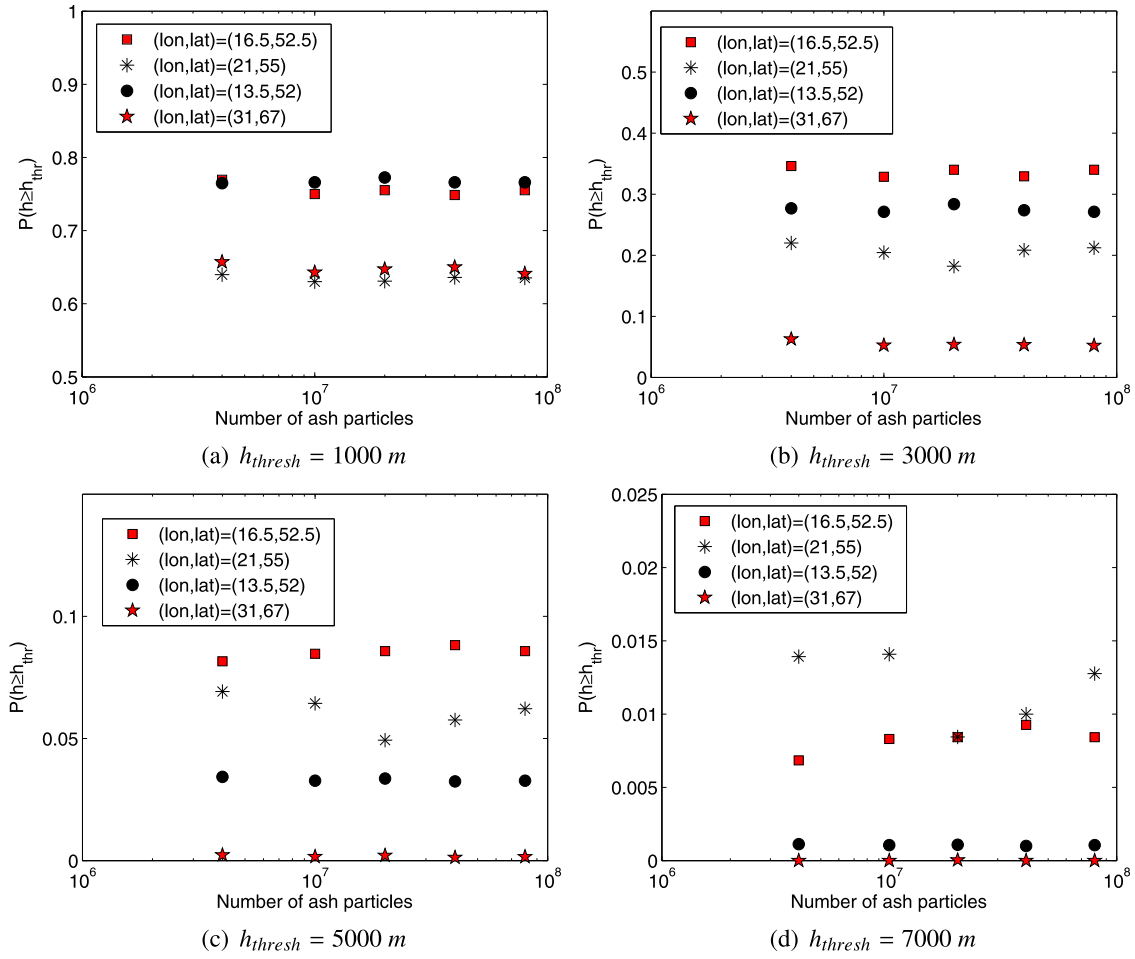


**Fig. 5.** Probability of ash top-height  $\geq h_{thresh}$  at different points on April 16th, 0600 hrs.

served height, so the sensor noise  $\nu_k$  is taken to be a zero-mean uniform density function over the interval  $[-100, 100]$  m. Due to height quantization in the bent-puff model, ash top-height provided by bent-puff model is assumed to be polluted with zero-mean uniformly distributed random noise between  $-1000$  m and  $+1000$  m. Thus  $\mathbf{Q}_k$  in Eq. (16) is taken to be  $3.33 \times 10^{-1} \text{ km}^2$  in our simulations.  $4 \times 10^7$  ash particles were used in the bent-puff model to compute different expectation integrals involved in the calculation of posterior source parameter distributions. To reduce the potential source of numerical error, PETSc [45] with two level domain decomposition based preconditioning (block Jacobi or Additive Schwarz) is used to compute the inverse involved in the computation of  $\mathbf{K}_k$  in Eq. (16).

The prior mean and standard deviation of ash top-height are shown in Fig. 10. Fig. 11 shows the posterior mean of the source parameters computed through Eq. (14), versus the number of satellite images considered in calculations of posterior mean and covariance. The expected source parameter values converge as more and more observational data are made available. Fig. 12 shows the assumed prior source parameter distributions and the computed posterior distributions based on satellite imagery for all three time-intervals. As expected, the uncertainty in source parameters decreases after the assimilation of satellite imagery. Because vent radius and eruption velocity directly control mass eruption rate, thermal flux and therefore eruption plume height, the fact that the cloud top height estimated from satellite data changes these values is intuitive. The effect of the satellite data on the grain size distribution is less obvious, but nevertheless can be easily understood when one remembers that the particles are settling, and the settling is a function of grain size. The large increase in the standard deviation of the grain size distribution would furthermore seem to be a reflection that the posterior estimate requires a greater number of fine-grained particles that settle only slowly.

Finally, the quality of the source parameter estimates is assessed by performing a single deterministic run of bent-puff corresponding to the estimated posterior mean of source parameters and comparing it against satellite observed ash top-height. Fig. 13(a) shows the ash top-height forecast at time 1200 hrs on April 16th using posterior estimates for source parameters obtained through incorporating satellite observation available at 600 hrs on April 16th. Similarly, Fig. 14(a) shows the ash top-height forecast at time 1800 hrs, obtained through incorporating satellite observations available at 600 hrs and 1200 hrs. Fig. 13(b) and Fig. 14(b) show the satellite observed ash top-height at 600 hrs and 1200 hrs, respectively. These results indicate that the forecast of ash cloud top-height based on the posterior estimate of source parameters matches very well with the observed satellite data. The observed and computed ash top-height differ from each other with an accuracy of  $\pm 2$  km, which corresponds to the numerical accuracy of bent-puff model.

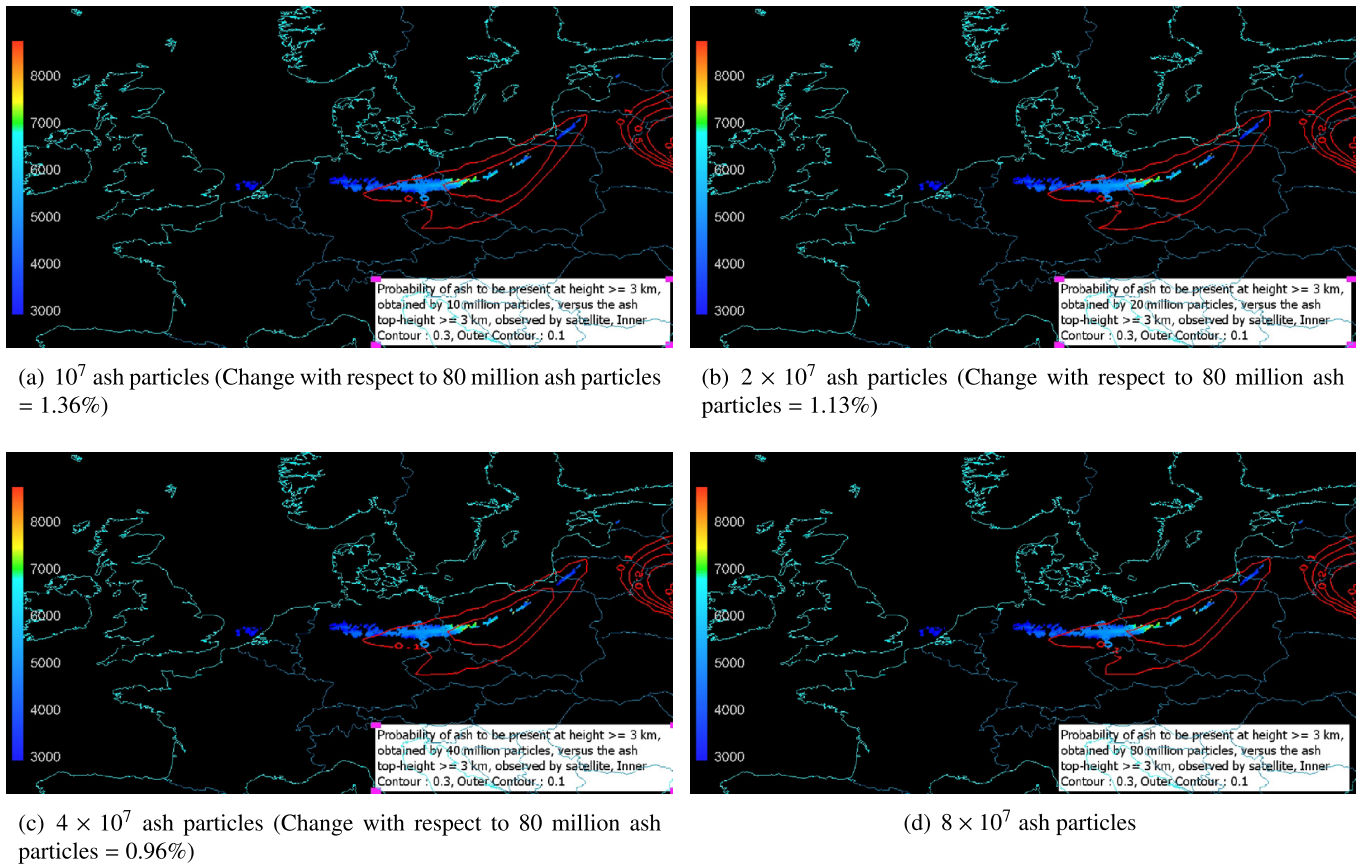


**Fig. 6.** Probability of ash top-height  $\geq 3$  km versus satellite observed ash top-height  $\geq 3$  km on April 16th, 1200 hrs (60 hours after eruption).

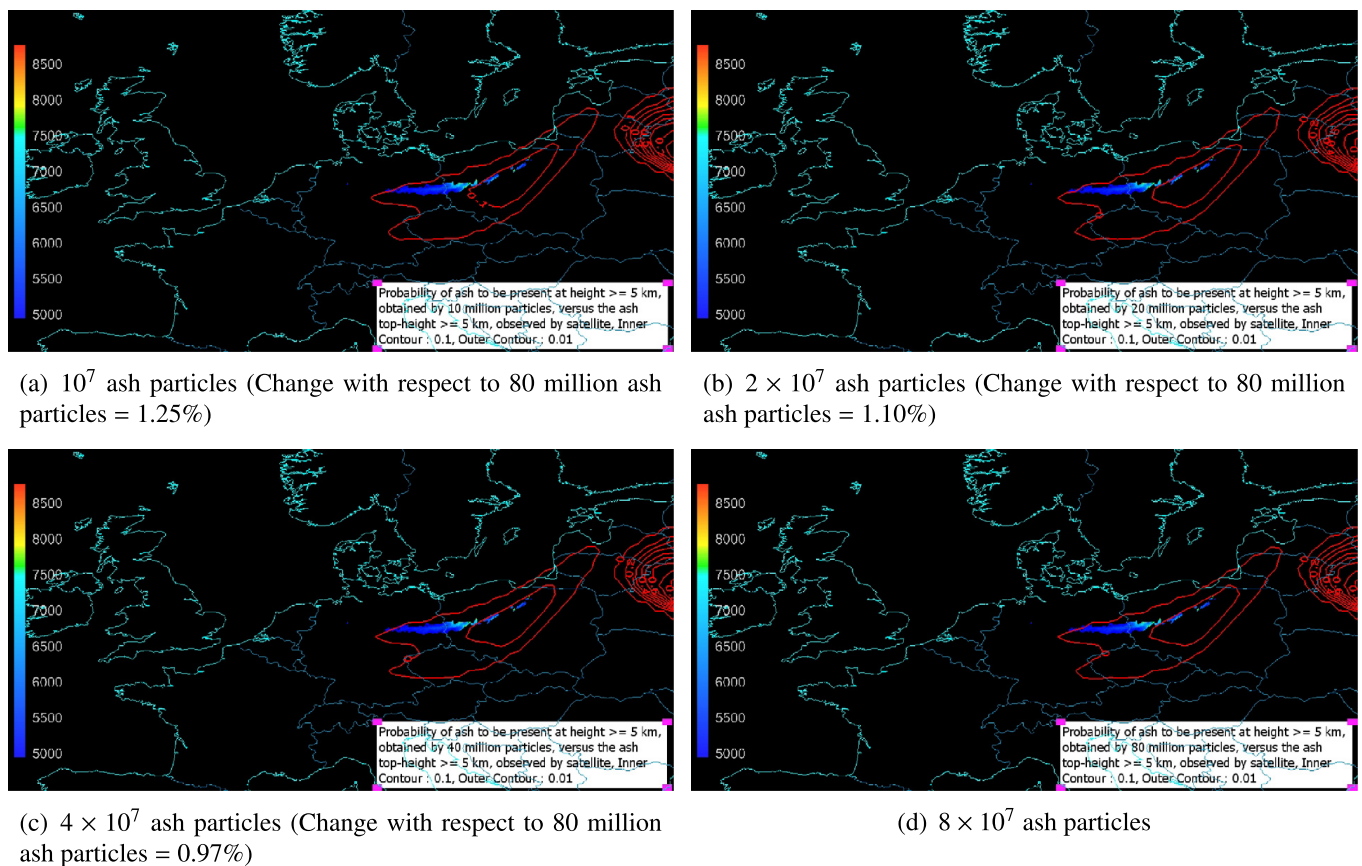


**Fig. 7.** Probability of ash top-height  $\geq 5$  km versus satellite observed ash top-height  $\geq 5$  km on April 16th, 1200 hrs (60 hours after eruption).

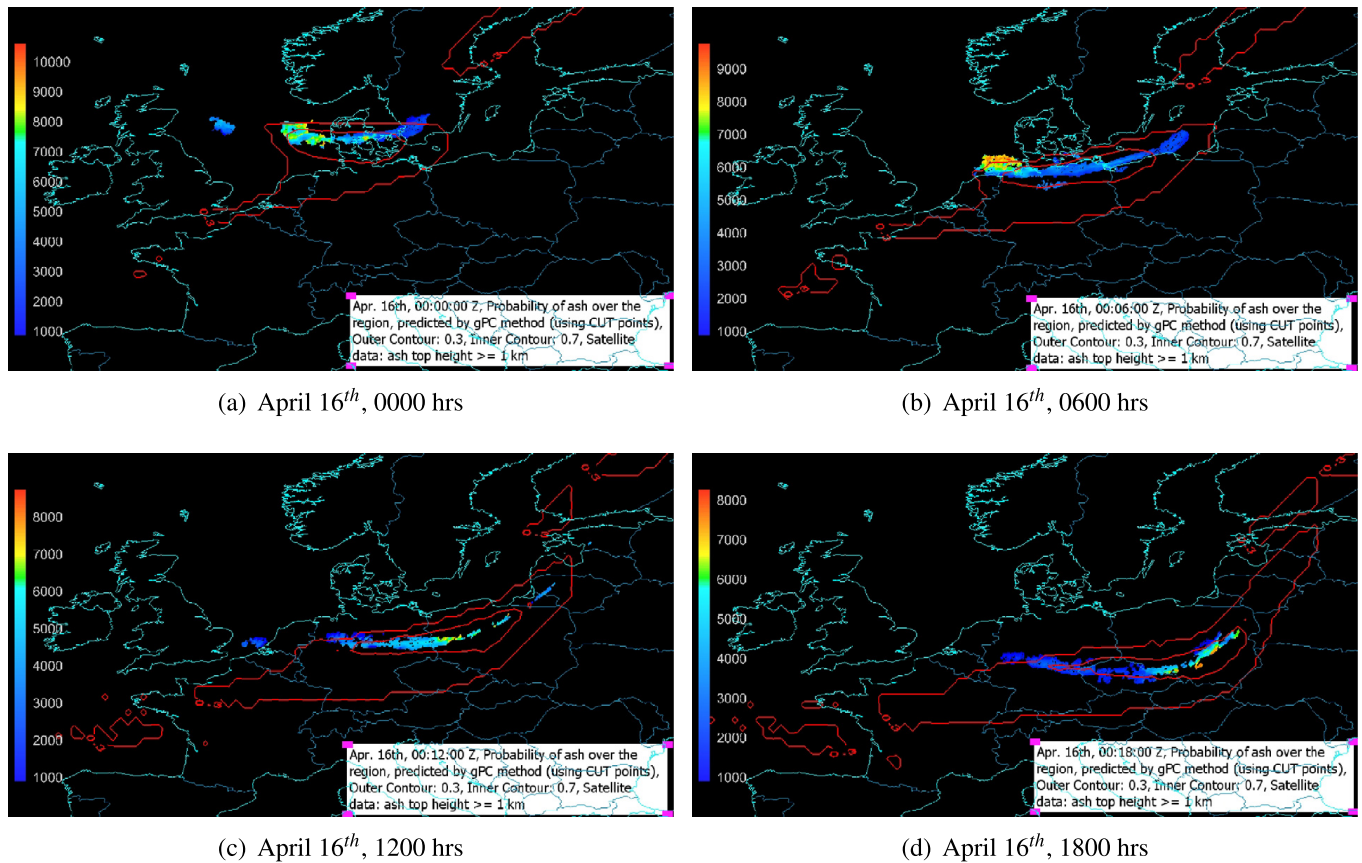


**Fig. 8.** Probability maps for ash top-height  $\geq 1$  km and corresponding satellite observed ash top-height.

### 5.3. Validation of posterior estimate of source parameters

The prior values for the source parameters used in this study were estimated based on the limited data that was available immediately following the eruption, and provided only a rough guide to true values, but nevertheless reflect the type of data that may be available at the time of eruption. Since the eruption, further studies have been completed and better estimates of the source parameters have become available. We compare these independent estimates of source parameters with the posterior mean estimates obtained here and reported in Table 4.

The vent radius was estimated from an airborne IMO radar image of the Earth's surface in the summit region taken on 14 April 2010 at 1030 UTC during the paroxysmal phase of the eruption, based on our own image analysis. Radar imagery is useful for this because of the ability of radio waves to penetrate eruption clouds. We originally assumed three of the darkest areas on the image to be craters. Later image guidance provided by the Icelandic Institute of Earth Sciences ([http://earthice.hi.is/eruption\\_eyjafjallajokull\\_2010](http://earthice.hi.is/eruption_eyjafjallajokull_2010)), however, suggests the presence of five roughly elliptical craters at that time, ranging in equivalent circular radius from 21 to 119 m (Table 4). Assuming that pressure balance in the plume as it exited the crater(s) developed rapidly based on the lack of atmospheric shocks in videography, and that crater diameter reflects pressure balance, the posterior estimate of 87 m eruption radius suggests that one of the two larger craters was active during the paroxysmal phase of the eruption on the morning of 14 April. This result is consistent with observations from other eruptions that vent activity migrates with time, and that the active vent during the most vigorous phase of an eruption should be that which allows the greatest flux. Measures of the initial velocity are now available for the initial, vigorous 14–18 April phase of the eruption based on a video of the erupting plume that was analyzed using a vortex tracking algorithm. The velocity near the vent was found to correlate with the relative vigor of the discharge from the volcano and plume height, and estimated to be 20–30 m/s on 17 April [57]. Given that this measurement was made slightly above the vent on the outer margin of the plume, in a rapidly decelerating section of the plume, it is probable that this observed velocity is slightly lower than the true exit velocity. The observed velocity of 20–30 m/s slightly above the vent thus is in accord with the mean value for the posterior mean exit velocity of 54 m/s, which is on the lower end of the prior range. The grain size distribution was studied mainly for the second intensive phase of the eruption (early May), during which time activity was similar to that seen in the early phase from 14–18 April. From these observations, it was found that the mean grain size,  $Md_\phi$ , changed from  $-0.9$  to  $4.5\phi$  and the standard deviation,  $\sigma_\phi$ , from  $0.7$  to  $2.6\phi$  with distance from the vent for deposits from the cloud found on land [58]. In fact, at a distance of 44 km from the vent and for the next 12 km, the observations shown a quasi-constant mean size of  $4.5\phi$  and a  $\sigma_\phi$  of  $2.6$ . This distance is within one computational cell from the source, and therefore grain sizes measured there should represent initial conditions. Furthermore, once the size



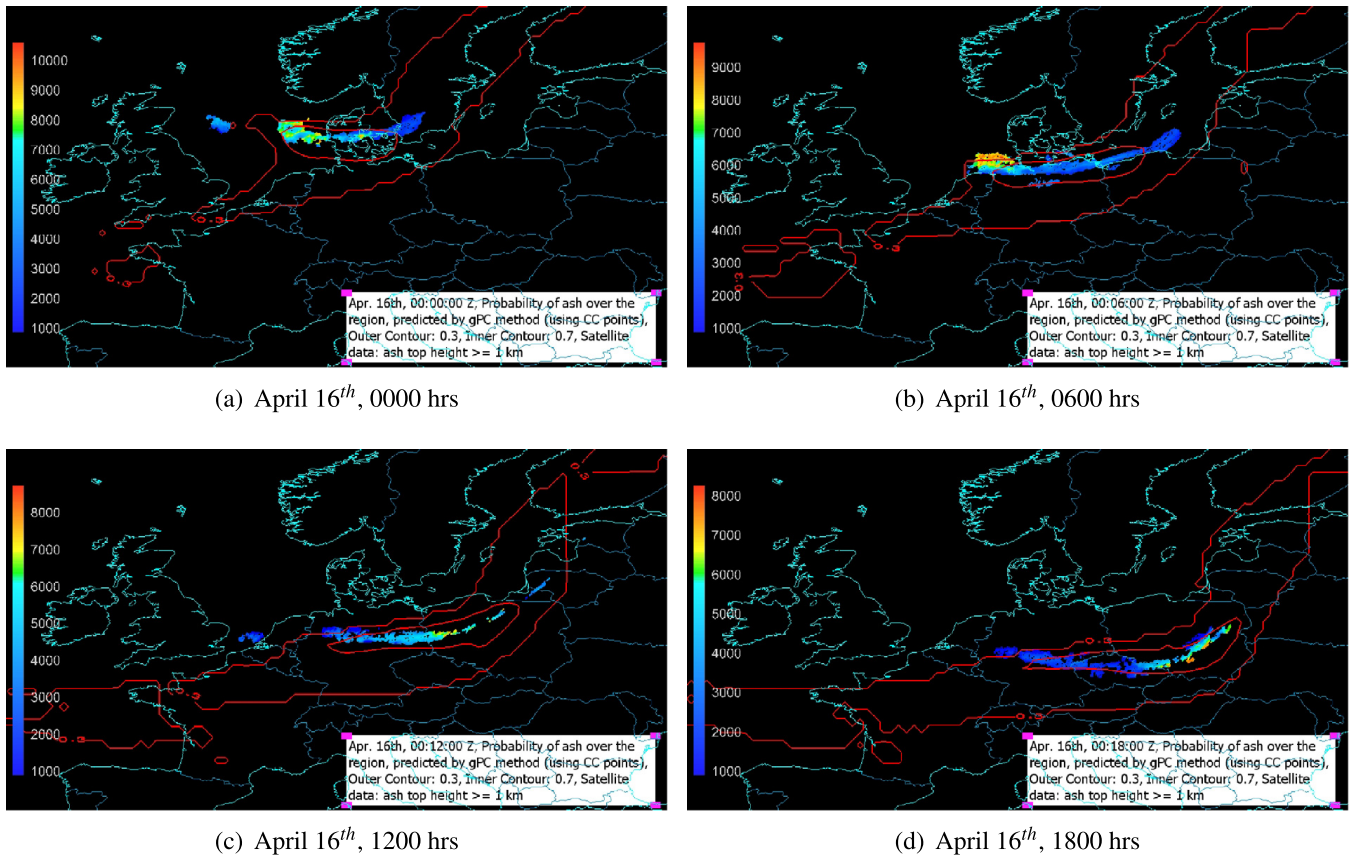


**Fig. 9.** Probability Maps (obtained through Clenshaw–Curtis quadrature scheme) for ash top-height  $\geq 1$  km and corresponding satellite observed ash top-height.

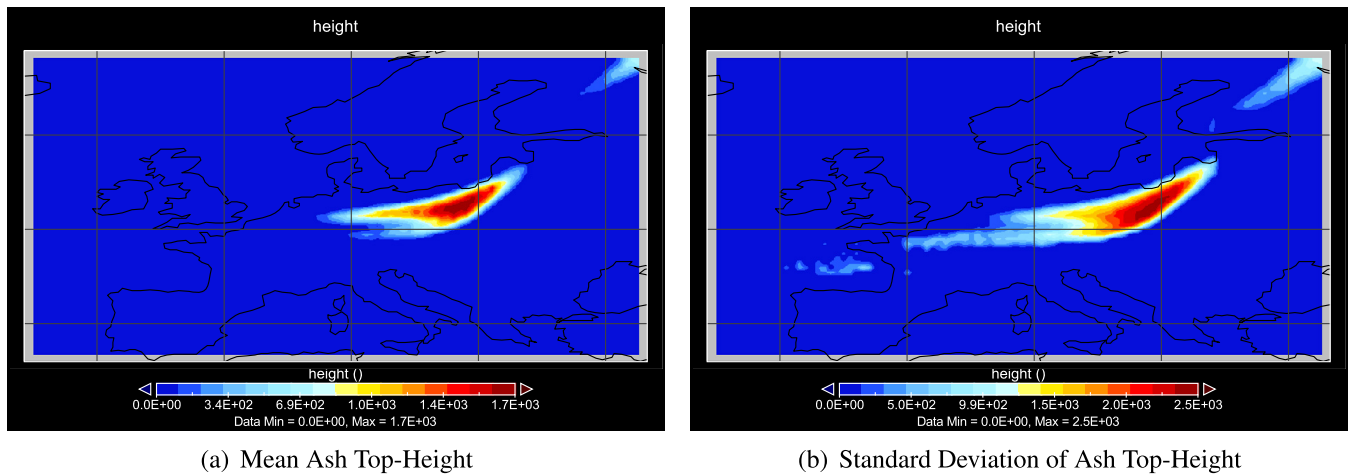


**Fig. 10.** Mean and standard deviation of ash top-height on April 16th, 1200 hrs.

of grains falling to the ground becomes constant, it can be assumed that the depositing grain size reflects the grain size of particles left in the cloud. If these assumptions are valid, the posterior estimate of the initial grain size distribution of  $4.96 \pm 2.62\phi$  correlates well with the measured value of  $4.5 \pm 2.6\phi$ .

## 6. Conclusion

In this article, an end-to-end approach to probabilistic forecasting of volcanic ash transport is outlined. Recently developed CUT quadrature method is used to propagate parameter uncertainty through the bent-puff model. The CUT ensembles are then used to construct a polynomial chaos surrogate model which is then sampled to provide probabilistic hazard map for ash top-height. Furthermore, the CUT method in conjunction with the minimum variance unbiased linear estimation approach is used to fuse bent-puff model forecasts and satellite observational data, to find a posterior

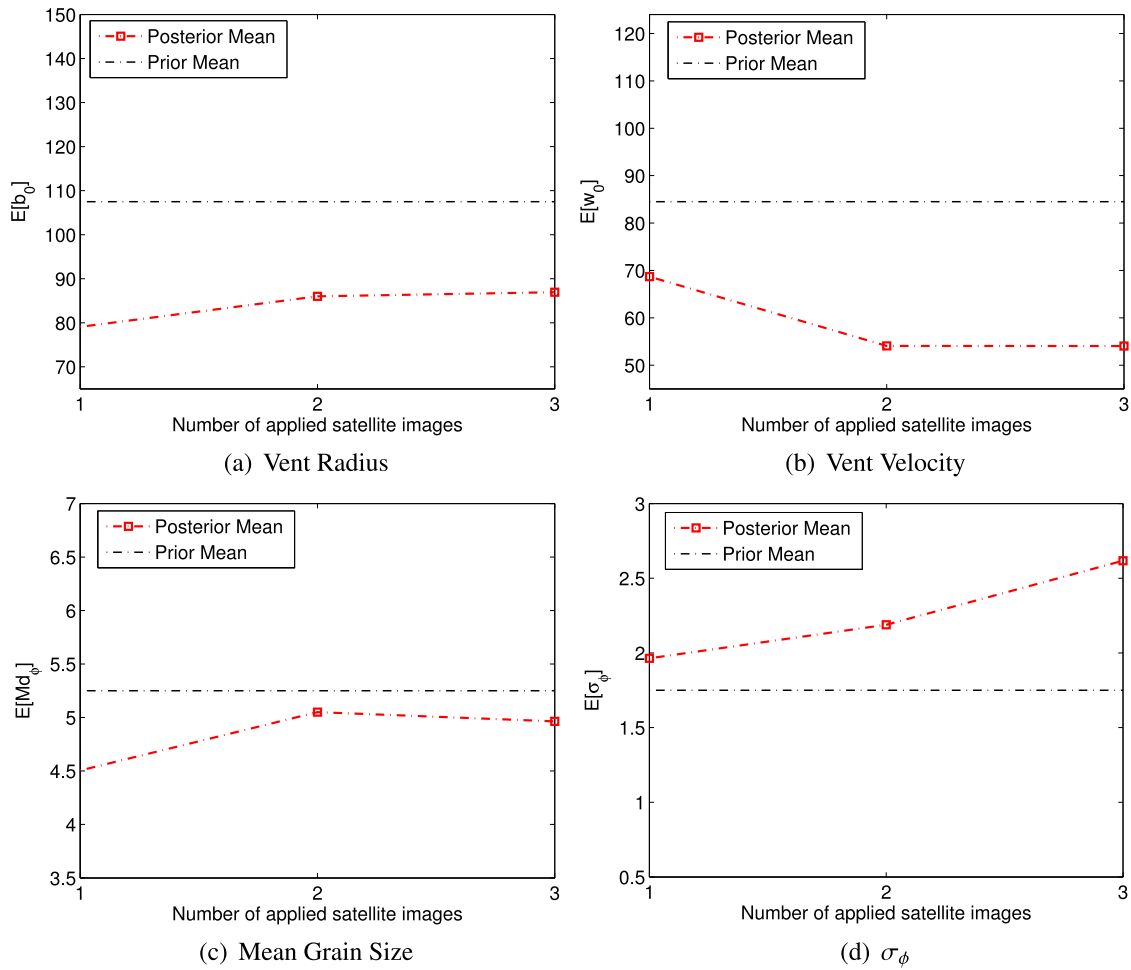


Fig. 11. Posterior mean estimates for source parameters versus number of ash particles.

estimate of source parameters and to update coefficients of polynomial chaos surrogate model. The updated polynomial chaos surrogate model is used to obtain posterior distribution of source parameters. This methodology is implemented and validated using the 2010 Eyjafjallajökull volcanic eruption as a benchmark problem. Numerical simulations illustrate the computational efficiency of using the CUT method. The source parameter estimation method proposed here provides not only mean estimates, but also a statistical confidence bound for that mean. Validation of the simulation results shows that the posterior estimate of source parameters corresponds well with values obtained in other references. Hazard maps based on our approach accurately forecast the location of ash, when tested against satellite data.

In this work, we have used the NOAA NCEP reanalysis 1 wind field to compute the hazard map. The reanalysis wind field uses observation data to produce a “best” known realization of the wind field consistent with data. Uncertainty in the wind forecast from the NWP model is significant, and incorporating this uncertainty into an enhanced model ensemble is the subject of ongoing work.

Finally, it is important to note that the overall framework for probabilistic model forecast and source estimation described here is not dependent on the choice of VATD or eruption model; other models can easily be used to generate column and plume outputs that are used in the subsequent uncertainty analysis.

## Acknowledgement

This material is based upon work jointly supported through National Science Foundation (NSF) under Awards Nos. CMMI-1131074, CMMI-1054759 and Air Force Office of Scientific Research (AFOSR) grant number FA9550-11-1-0336. All results and opinions expressed in this article are those of the authors and do not reflect opinions of NSF or AFOSR.

## Appendix A. 8th order CUT quadrature points

In this appendix, the procedure to obtain 8th order Conjugate Unscented Transform (CUT) quadrature points for a uniform pdf in 4-dimensional space is explained in detail. According to the procedure explained in Section 4.1, the main steps can be described as follows:



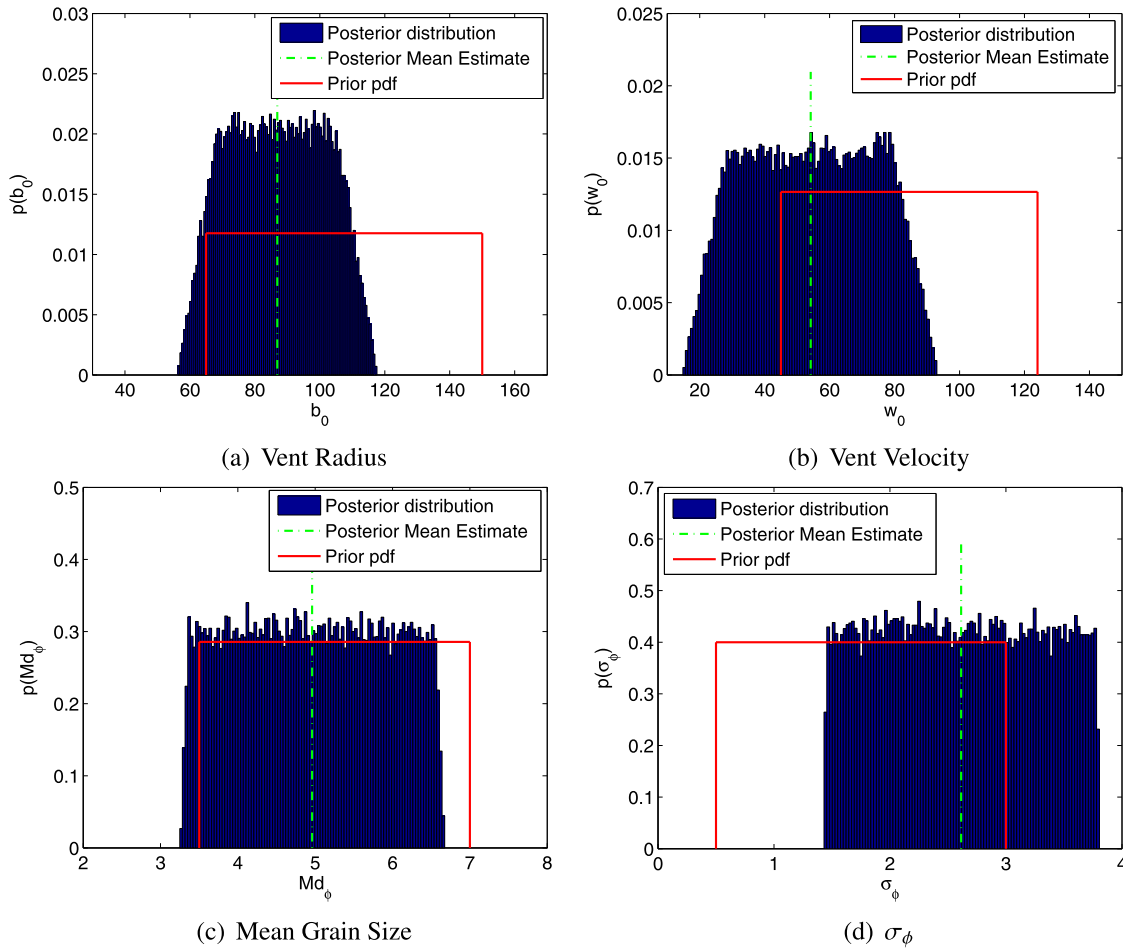


Fig. 12. Prior and posterior estimate of source parameters.

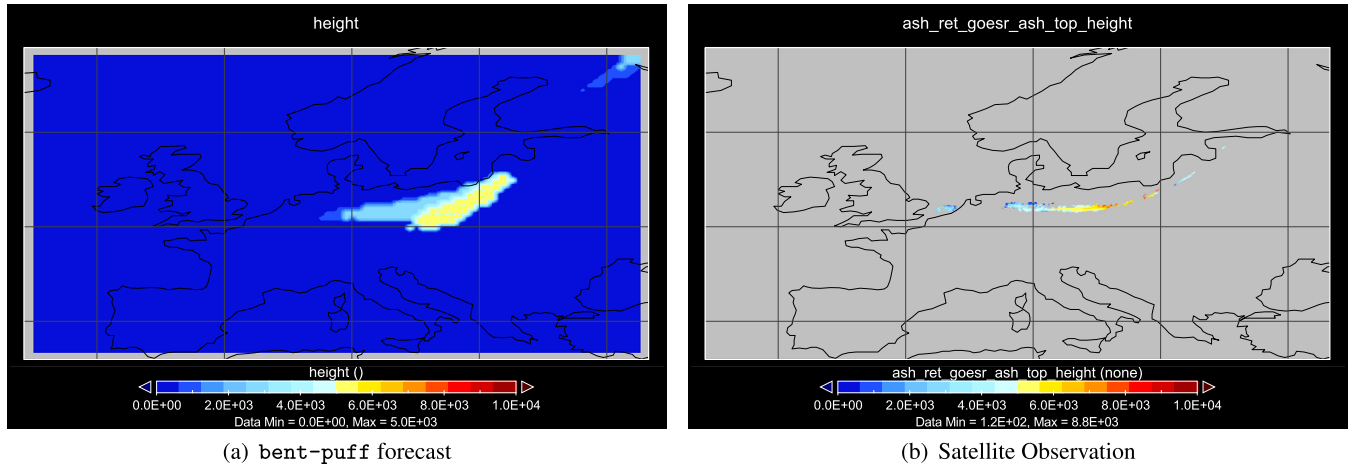


Fig. 13. Comparison of forecast of ash top-height and satellite observation on April 16th, 1200 hrs.

- The first set of points are selected on the principal axis. Note that there will be  $2N = 8$  points on principal axes which all have the same distance from the origin and their weights are all the same, i.e.  $X_i^{(1)} = r_1 \sigma_i$  and  $W_i^{(1)} = w_1$ .
- The second set of points are contained to lie on the 4th-conjugate axis. There will be  $2^4 \binom{4}{4} = 16$  points on 4th-conjugate axis which all have the same distance from the origin, i.e.  $X_i^{(2)} = r_2 c_i^4$ . Also, they all will have equal weight  $w_2$ .
- The third set of points are assumed to lie on the 2nd-conjugate axis. Note that there exist  $2^2 \binom{4}{2} = 24$  points on 2nd-conjugate axis. Similar to previous points, these points are also equidistant from the origin and have the same weight, i.e.  $X_i^{(3)} = r_3 c_i^2$  and  $W_i^{(3)} = w_3$ .

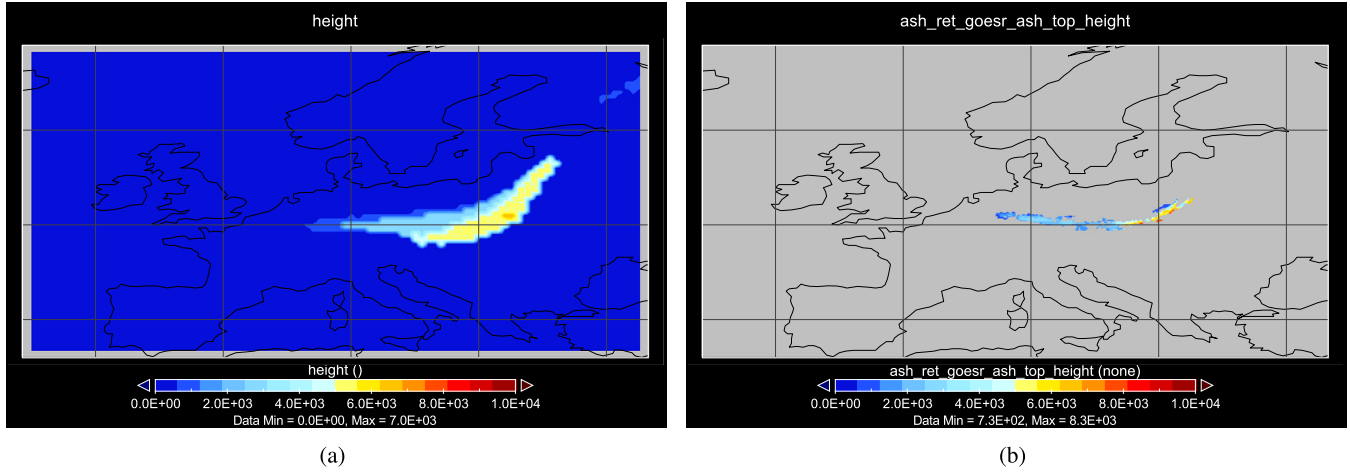


Fig. 14. Comparison of forecast of ash top-height and satellite observation on April 16th, 1800 hrs.

Table 4

Comparison of prior, posterior and new estimates of eruption source parameters based on observations of Eyjafjallajökull eruption and simulations.

Parameter	Prior range	Posterior mean	New	Reference
Vent radius, $b_0$ (m)	65–150	87	21, 65, 119, 31, 32	Remeasured based on better image guidance
Vent velocity, $w_0$ (m/s)	45–124	54	>20–30	[57]
Mean grain size, $Md_\varphi$ ( $\varphi$ )	3.5–7	4.96	4.5	[58]
$\sigma_\varphi, \varphi$	0.5–3	2.62	2.6	[58]

Note that the grain size unit of geology,  $\varphi$ , is defined as:  $\varphi = -\log_2(D/D_0)$ , where diameter,  $D$ , is measured in mm, and reference diameter  $D_0 = 1$  mm.

- Like the second set of points, the fourth set of points are assumed to lie on the 4th-conjugate axis. Hence, there will be another set of  $2^4 \binom{4}{4} = 16$  points on 4th-conjugate axis. But, they will have different distance from the origin, i.e.  $X_i^{(4)} = r_4 c_i^4$ , where  $r_4 \neq r_2$ . As well, all the  $X_i^{(4)}$ 's are considered to have the same weight  $w_4 \neq w_2$ .
- The other set of points are assumed lie on the 3rd-conjugate axis such that  $X_i^{(5)} = r_5 c_i^3$  and  $W_i^{(5)} = w_5$ . Note that there will be  $2^3 \binom{4}{3} = 32$  points on 3rd-conjugate axis.
- The last set of points are located on 4th-scaled conjugate axis, i.e.  $X_i^{(6)} = r_6 s_i^N(h)$  and  $W_i^{(6)} = w_6$ , where the scaling parameter  $h$  needs to be appropriately selected.

There will be totally 161 quadrature points (those just described plus the origin) whose locations can be determined by finding the values of  $r_j$ 's ( $j = 1, 2, \dots, 6$ ). To find the values of  $w_0, r_j$ 's and  $w_j$ 's ( $j = 1, 2, \dots, 6$ ), one needs to construct and solve the moment constraint equations. Due to the symmetrical properties of the selected points, the odd order central moments are automatically satisfied, and one only needs to satisfy the even order central moments:

$$\begin{cases} \mathbb{E}[x_i^2] = \frac{1}{3}, & \mathbb{E}[x_i^4] = \frac{1}{4}, & \mathbb{E}[x_i^2 x_j^2] = \frac{1}{9} \\ \mathbb{E}[x_i^6] = \frac{1}{7}, & \mathbb{E}[x_i^4 x_j^2] = \frac{1}{15}, & \mathbb{E}[x_i^2 x_j^2 x_k^2] = \frac{1}{27} \\ \mathbb{E}[x_i^8] = \frac{1}{9}, & \mathbb{E}[x_i^6 x_j^2] = \frac{1}{21}, & \mathbb{E}[x_i^4 x_j^4] = \frac{1}{25} \\ \mathbb{E}[x_i^4 x_j^2 x_k^2] = \frac{1}{45}, & \mathbb{E}[x_i^2 x_j^2 x_k^2 x_l^2] = \frac{1}{81}, & \int_{\Omega} p(x_1, x_2, x_3, x_4) d\mathbf{x} = 1 \end{cases} \quad (\text{A.1})$$

The last equation ensures the unity constraint and  $\Omega = [-1, +1]^4 \subset \mathbb{R}^4$ . Eq. (A.2) shows the moment constraints equations in terms of selected conjugate unscented points and their corresponding weights. Eq. (A.2) is a set of 12 nonlinear equations with 13 unknowns, viz.  $w_0, w_j$ 's and  $r_j$ 's ( $j = 1, 2, \dots, 6$ ).

**Table A.5**

Values of  $r_i$ 's,  $w_i$ 's, and  $h$ , obtained by solving Eq. (A.2).

$r_1$	0.9185985004650354	$w_1$	0.008062125720404502
$r_2$	0.4056290098577023	$w_2$	0.014595344864200561
$r_3$	0.7897970163891953	$w_3$	0.013047011752780219
$r_4$	0.918231359082217	$w_4$	0.001790784328179888
$r_5$	0.5610319682295122	$w_5$	0.004699572845907843
$r_6$	0.8770580193070292	$w_6$	0.0006502632426480917
$h$	1.7		
$w_0$	0.02036722182060191		

$$\left\{ \begin{array}{l}
 2r_1^2 w_1 + 16r_2^2 w_2 + 12r_3^2 w_3 + 24r_4^2 w_4 + 48r_5^2 w_5 + 16h2r_5^2 w_5 + 16r_6^2 w_6 = \frac{1}{3} \\
 2r_1^4 w_1 + 16r_2^4 w_2 + 12r_3^4 w_3 + 24r_4^4 w_4 + 48r_5^4 w_5 + 16h4r_5^4 w_5 + 16r_6^4 w_6 = \frac{1}{5} \\
 16r_2^4 w_2 + 4r_3^4 w_3 + 16r_4^4 w_4 + 32r_5^4 w_5 + 32h2r_5^4 w_5 + 16r_6^4 w_6 = \frac{1}{9} \\
 2r_1^6 w_1 + 16r_2^6 w_2 + 12r_3^6 w_3 + 24r_4^6 w_4 + 48r_5^6 w_5 + 16h6r_5^6 w_5 + 16r_6^6 w_6 = \frac{1}{7} \\
 16r_2^6 w_2 + 4r_3^6 w_3 + 16r_4^6 w_4 + 32r_5^6 w_5 + 16h2r_5^6 w_5 + 16h4r_5^6 w_5 + 16r_6^6 w_6 = \frac{1}{15} \\
 16r_2^6 w_2 + 8r_4^6 w_4 + 16r_5^6 w_5 + 48h2r_5^6 w_5 + 16r_6^6 w_6 = \frac{1}{27} \\
 2r_1^8 w_1 + 16r_2^8 w_2 + 12r_3^8 w_3 + 24r_4^8 w_4 + 48r_5^8 w_5 + 16h8r_5^8 w_5 + 16r_6^8 w_6 = \frac{1}{9} \\
 16r_2^8 w_2 + 4r_3^8 w_3 + 16r_4^8 w_4 + 32r_5^8 w_5 + 16h2r_5^8 w_5 + 16h6r_5^8 w_5 + 16r_6^8 w_6 = \frac{1}{21} \\
 16r_2^8 w_2 + 4r_3^8 w_3 + 16r_4^8 w_4 + 32r_5^8 w_5 + 32h4r_5^8 w_5 + 16r_6^8 w_6 = \frac{1}{25} \\
 16r_2^8 w_2 + 8r_4^8 w_4 + 16r_5^8 w_5 + 32h2r_5^8 w_5 + 16h4r_5^8 w_5 + 16r_6^8 w_6 = \frac{1}{45} \\
 16r_2^8 w_2 + 64h2r_5^8 w_5 + 16r_6^8 w_6 = \frac{1}{81} \\
 w_0 + 8w_1 + 16w_2 + 24w_3 + 32w_4 + 64w_5 + 16w_6 = 1
 \end{array} \right. \quad (A.2)$$

To find a unique solution  $w_0$ ,  $w_j$ 's and  $r_j$ 's, minimize the error for this system. Table A.5 represents the values for  $r_i$ 's,  $w_i$ 's obtained by solving Eq. (A.2).

## References

- [1] D. Schneider, W. Rose, L. Kelley, Tracking of 1992 eruption clouds from Crater Peak vent of Mount Spurr Volcano, Alaska using AVHRR, U.S. Geol. Surv. Bull. 2139 (1995) 27–36.
- [2] K. F. 867, [http://en.wikipedia.org/wiki/KLM\\_Flight\\_867](http://en.wikipedia.org/wiki/KLM_Flight_867).
- [3] CNN, New ash cloud could extend air travel threat, accessed at <http://www.cnn.com/2010/TRAVEL/04/19/volcano.ash/index.html>.
- [4] N. Adurthi, The conjugate unscented transform – a method to evaluate multidimensional expectation integrals, Master's thesis, University at Buffalo.
- [5] A. Nagavenkat, P. Singla, T. Singh, The conjugate unscented transform—an approach to evaluate multi-dimensional expectation integrals, in: Proceedings of the American Control Conference, 2012.
- [6] A. Nagavenkat, P. Singla, T. Singh, Conjugate unscented transform rules for uniform probability density functions, in: Proceedings of the American Control Conference, 2013.
- [7] A. Nagavenkat, P. Singla, T. Singh, Conjugate unscented transform and its application to filtering and stochastic integral calculation, in: AIAA Guidance, Navigation, and Control Conference, 2012.
- [8] S. Gislason, H. Alfredsson, E. Eiriksdottir, T. Hassenkam, S. Stipp, Volcanic ash from the 2010 Eyjafjallajökull eruption, Appl. Geochem. 26 (Suppl.) (2011) S188–S190, <http://dx.doi.org/10.1016/j.apgeochem.2011.03.100>.
- [9] D.B. Ryall, R.H. Maryon, Validation of the UK Met. Office's name model against the ETEX dataset, Atmos. Environ. 32 (1998) 4265–4276.
- [10] B. Devenish, D. Thomson, F. Marenco, S. Leadbetter, H. Ricketts, H. Dacre, A study of the arrival over the United Kingdom in April 2010 of the Eyjafjallajökull ash cloud using ground-based LIDAR and numerical simulations, Atmos. Environ. 48 (2012) 152–164.
- [11] C. O'Dowd, S. Varghese, D. Martin, R. Flanagan, A. McKinstry, D. Ceburnis, J. O'vadnevaite, G. Martucci, J. Bialek, C. Monahan, H. Berresheim, A. Vaishya, T. Grigas, Z. McGraw, S. Jennings, B. Langmann, T. Semmler, R. McGrath, The Eyjafjallajökull ash plume part 2: Simulating ash cloud dispersion with REMOTE, Atmos. Environ. 48 (2012) 143–151, <http://dx.doi.org/10.1016/j.atmosenv.2011.10.037>.
- [12] P. Webley, T. Steensen, M. Stuefer, G. Grell, S. Freitas, M. Pavolonis, Analyzing the Eyjafjallajökull 2010 eruption using satellite remote sensing, lidar and WRF-Chem dispersion and tracking model, J. Geophys. Res., Atmos. 117 (D13) (2012).
- [13] B. Heinold, I. Tegen, R. Wolke, A. Ansmann, I. Mattis, A. Minikin, U. Schumann, B. Weinzierl, Simulations of the 2010 Eyjafjallajökull volcanic ash dispersal over Europe using COSMO-MUSCAT, Atmos. Environ. 48 (2012) 195–204.

- [14] A. Folch, A. Costa, S. Basart, Validation of the FALL3D ash dispersion model using observations of the 2010 Eyjafjallajökull volcanic ash clouds, *Atmos. Environ.* 48 (2012) 165–183.
- [15] A. Stohl, A. Prata, S. Eckhardt, L. Clarisse, A. Durant, S. Henne, N. Kristiansen, A. Minikin, U. Schumann, P. Seibert, et al., Determination of time-and height-resolved volcanic ash emissions and their use for quantitative ash dispersion modeling: the 2010 Eyjafjallajökull eruption, *Atmos. Chem. Phys.* 11 (9) (2011) 4333–4351.
- [16] R.P. Denlinger, M. Pavlonis, J. Sieglaff, A robust method to forecast volcanic ash clouds, *J. Geophys. Res., Atmos.* 117 (D13) (2012), <http://dx.doi.org/10.1029/2012JD017732>.
- [17] N.I. Kristiansen, A. Stohl, A.J. Prata, N. Bukowiecki, H. Dacre, S. Eckhardt, S. Henne, M.C. Hort, B.T. Johnson, F. Marengo, B. Neininger, O. Reitebuch, P. Seibert, D.J. Thomson, H.N. Webster, B. Weinzierl, Performance assessment of a volcanic ash transport model mini-ensemble used for inverse modeling of the 2010 Eyjafjallajökull eruption, *J. Geophys. Res., Atmos.* 117 (D20) (2012), <http://dx.doi.org/10.1029/2011JD016844>.
- [18] A.H. Jazwinski, *Stochastic Processes and Filtering Theory*, Academic Press, 1970.
- [19] H.W. Sorenson, *Parameter Estimation: Principles and Problems*, Marcel Dekker, New York, 1980.
- [20] N. Wiener, The homogeneous chaos, *Am. J. Math.* 60 (4) (1938) 897–936.
- [21] D. Xiu, G.E. Karniadakis, The Wiener–Askey polynomial chaos for stochastic differential equations, *SIAM J. Sci. Comput.* 24 (2) (2002) 619–644.
- [22] R.G. Ghanem, P.D. Spanos, *Stochastic Finite Elements: A Spectral Approach*, Springer-Verlag, New York, NY, 1991.
- [23] J. Li, D. Xiu, A generalized polynomial chaos based ensemble Kalman filter with high accuracy, *J. Comput. Phys.* 228 (15) (2009) 5454–5469, <http://dx.doi.org/10.1016/j.jcp.2009.04.029>.
- [24] Y.M. Marzouk, H.N. Najm, L.A. Rahn, Stochastic spectral methods for efficient Bayesian solution of inverse problems, *J. Comput. Phys.* 224 (2) (2007) 560–586, <http://dx.doi.org/10.1016/j.jcp.2006.10.010>.
- [25] R. Madankan, P. Singla, T. Singh, P. Scott, Polynomial chaos based Bayesian approach for state and parameter estimation, *J. Guid. Control Dyn.* 36 (4) (2013) 1058–1074.
- [26] T. Gerstner, M. Griebel, Numerical integration using sparse grids, *Numer. Algorithms* 18 (1998) 209–232, <http://dx.doi.org/10.1023/A:1019129717644>.
- [27] A.H. Stroud, D. Secrest, *Gaussian Quadrature Formulas*, Prentice Hall, Englewood Cliffs, NJ, 1966.
- [28] M. Bursik, M. Jones, S. Carn, K. Dean, A. Patra, M. Pavlonis, E.B. Pitman, T. Singh, P. Singla, P. Webley, et al., Estimation and propagation of volcanic source parameter uncertainty in an ash transport and dispersal model: application to the Eyjafjallajökull plume of 14–16 April 2010, *Bull. Volcanol.* (2012) 1–18.
- [29] S. Carey, R. Sparks, Quantitative models of the fallout and dispersal of tephra from volcanic eruption columns, *Bull. Volcanol.* 48 (1986) 109–125.
- [30] T. Suzuki, *A Theoretical Model for Dispersion of Tephra*, Terra Scientific Publishing, Tokyo, 2005, pp. 95–116.
- [31] H. Tanaka, Development of a prediction scheme for the volcanic ash fall from redoubt volcano, in: *First Int'l Symposium on Volcanic Ash and Aviation Safety*, Seattle, 1991, p. 58.
- [32] C. Searcy, K. Dean, B. Stringer, PUFF: A volcanic ash tracking and prediction model, *J. Volcanol. Geotherm. Res.* 80 (1998) 1–16.
- [33] P. Webley, K. Dean, J. Dehn, J. Bailey, R. Peterson, Volcanic ash dispersion modeling of the 2006 eruption of Augustine Volcano, USGS Professional Paper: Augustine Volcano 2006 eruption.
- [34] L. Mastin, M. Guffanti, R. Servanckx, P. Webley, S. Barsotti, K. Dean, R. Denlinger, A. Durant, J. Ewert, C. Gardner, A. Holliday, A. Neri, W. Rose, D. Schneider, L. Siebert, B. Stunder, G. Swanson, A. Tupper, A. Volentik, A. Waythomas, A multidisciplinary effort to assign realistic source parameters to models of volcanic ash-cloud transport and dispersion during eruptions, in: L. Mastin, P.W. Webley (Eds.), *Special Issue on Volcanic Ash Clouds*, *J. Volcanol. Geotherm. Res.* 186 (2009) 10–21.
- [35] R.S.J. Sparks, M.I. Bursik, S.N. Carey, J.S. Gilbert, L.S. Glaze, H. Sigurdsson, A.W. Woods, *Volcanic Plumes*, John Wiley & Sons, London, 1997, 574 pp.
- [36] M. Bursik, S. Kobs, A. Burns, O. Braitseva, L. Bazanova, I. Melekestsev, A. Kurbatov, D. Pieri, Volcanic plumes and the wind: jetstream interaction examples and implications for air traffic, *J. Volcanol. Geotherm. Res.* 186 (2009) 60–67.
- [37] M. Bursik, Effect of wind on the rise height of volcanic plumes, *Geophys. Res. Lett.* 18 (2001) 3621–3624.
- [38] B. Morton, J. Turner, G. Taylor, Gravitational turbulent convection from maintained and instantaneous sources, *Proc. R. Soc. Lond. Ser. A* 234 (1956) 1–23.
- [39] K. Dalbey, A. Patra, E. Pitman, M. Bursik, M. Sheridan, Input uncertainty propagation methods and hazard mapping of geophysical mass flows, *J. Geophys. Res.* 113 (2008), B05203.
- [40] O. LeMaitre, O. Knio, H. Najm, R. Ghanem, A stochastic projection method for fluid flow: I. Basic formulation, *J. Comput. Phys.* 173 (2001) 481–511.
- [41] D. Xiu, J. Hesthaven, High-order collocation methods for differential equations with random inputs, *SIAM J. Sci. Comput.* 27 (2005) 1118–1139.
- [42] M. Berveiller, B. Sudret, M. Lemaire, Stochastic finite element: a non intrusive approach by regression, *Rev. Eur. Mec. Numer.* 15 (2006) 81–92.
- [43] A. Gelb, *Applied Optimal Estimation*, MIT Press, 1974.
- [44] T. Gerstner, M. Griebel, Numerical integration using sparse grids, *Numer. Algorithms* 18.
- [45] S. Balay, J. Brown, K. Buschelman, V. Eijkhout, W. Gropp, D. Kaushik, M. Knepley, L. C. McInnes, B. Smith, H. Zhang, *Petsc users manual revision 3.3*.
- [46] National Center for Environmental Prediction, Unidata online access to the operational Global Forecasting System (GFS) numerical weather prediction model, [http://motherlode.ucar.edu:8080/thredds/catalog/fmrc/NCEP/GFS/Global\\_Op5deg/catalog.html](http://motherlode.ucar.edu:8080/thredds/catalog/fmrc/NCEP/GFS/Global_Op5deg/catalog.html), 2009.
- [47] National Center for Environmental Prediction, Unidata online access to the operational North American Mesoscale (NAM) numerical weather prediction model, [http://motherlode.ucar.edu:8080/thredds/catalog/fmrc/NCEP/NAM/Alaska\\_11km/catalog.html](http://motherlode.ucar.edu:8080/thredds/catalog/fmrc/NCEP/NAM/Alaska_11km/catalog.html), 2009.
- [48] United States Navy Fleet Numerical Meteorology and Oceanography Center, online access to the Navy Operational Global Atmospheric Prediction System numerical weather prediction model, <https://www.fnmoc.navy.mil/public>, 2009.
- [49] T.W. Research, Forecasting, <http://www.wrf-model.org/index.php>.
- [50] M. Ripepe, S.D. Angelis, G. Lacanna, B. Voight, Observation of infrasonic and gravity waves at Soufrière Hills Volcano, Montserrat, *Geophys. Res. Lett.* 37 (2010) L00E14, <http://dx.doi.org/10.1029/2010GL042557>.
- [51] A.W. Woods, M.I. Bursik, Particle fallout, thermal disequilibrium and volcanic plumes, *Bull. Volcanol.* 53 (1991) 559–570.
- [52] M.J. Pavlonis, W.F. Feltz, A.K. Heidinger, G.M. Gallina, A daytime complement to the reverse absorption technique for improved automated detection of volcanic ash, *J. Atmos. Ocean. Technol.* 23 (2006) 1422–1444.
- [53] M.J. Pavlonis, Advances in extracting cloud composition information from spaceborne infrared radiances: A robust alternative to brightness temperatures. Part I: Theory, *J. Appl. Meteorol. Climatol.* 49 (2010) 1992–2012.
- [54] A.K. Heidinger, M.J. Pavlonis, Nearly 30 years of gazing at cirrus clouds through a split-window. Part I: Methodology, *J. Appl. Meteorol. Climatol.* 48 (2009) 1110–1116.
- [55] A.K. Heidinger, M.J.P.R.E. Holz, B.A. Baum, S. Berthier, Using CALIPSO to explore the sensitivity to cirrus height in the infrared observations from NPOESS/VIIIRS and GOES-R/ABI, *J. Geophys. Res., Atmos.* 115 (2010), <http://dx.doi.org/10.1029/2009JD012152>.
- [56] S. Scollo, M. Prestifilippo, M. Coltell, R. Peterson, G. Spata, A statistical approach to evaluate the tephra deposit and ash concentration from {PUFF} model forecasts, *J. Volcanol. Geotherm. Res.* 200 (3–4) (2011) 129–142, <http://dx.doi.org/10.1016/j.jvolgeores.2010.12.004>, <http://www.sciencedirect.com/science/article/pii/S0377027310003823>.
- [57] G. Petersen, H. Bojornsson, P. Arason, The impact of the atmosphere on the Eyjafjallajökull 2010 eruption plume, *J. Geophys. Res., Atmos.* 117 (2012), <http://dx.doi.org/10.1029/2011JD016762>.
- [58] C. Bonadonna, R. Genco, M. Gouhier, M. Pistolesi, R. Cioni, F. Alfano, A. Hoskuldsson, M. Ripepe, Tephra sedimentation during the 2010 Eyjafjallajökull eruption (Iceland) from deposit, radar and satellite observations, *J. Geophys. Res., Solid Earth* 116 (2011), <http://dx.doi.org/10.1029/2011JB008462>.